Scaling of Off-Equatorial Jets in Giant Planet Atmospheres

JUNJUN LIU

California Institute of Technology, Pasadena, California

TAPIO SCHNEIDER

ETH Zürich, Zurich, Switzerland

(Manuscript received 7 December 2013, in final form 3 September 2014)

ABSTRACT

In the off-equatorial region of Jupiter's and Saturn's atmospheres, baroclinic eddies transport angular momentum out of retrograde and into prograde jets. In a statistically steady state, this angular momentum transfer by eddies must be balanced by dissipation, likely produced by magnetohydrodynamic (MHD) drag in the planetary interior. This paper examines systematically how an idealized representation of this drag in a general circulation model (GCM) of the upper atmosphere of giant planets modifies jet characteristics, the angular momentum budget, and the energy budget.

In the GCM, Rayleigh drag at an artificial lower boundary (with mean pressure of 3 bar) is used as a simple representation of the MHD drag that the flow on giant planets experiences at depth. As the drag coefficient decreases, the eddy length scale and eddy kinetic energy increase, as they do in studies of two-dimensional turbulence. Off-equatorial jets become wider and stronger, with increased interjet spacing. Coherent vortices also become more prevalent. Generally, the jet width scales with the Rhines scale, which is of similar magnitude as the Rossby radius in the simulations. The jet strength increases primarily through strengthening of the barotropic component, which increases as the drag coefficient decreases because the overall kinetic energy dissipation remains roughly constant. The overall kinetic energy dissipation remains roughly constant presumably because it is controlled by baroclinic conversion of potential to kinetic energy in the upper troposphere, which is mainly determined by the differential solar radiation and is only weakly dependent on bottom drag and barotropic flow variations.

For Jupiter and Saturn, these results suggest that the wider and stronger jets on Saturn may arise because the MHD drag on Saturn is weaker than on Jupiter, while the thermodynamic efficiencies of the atmospheres are not sensitive to the drag parameters.

1. Introduction

Jupiter's and Saturn's tropospheres exhibit alternating prograde and retrograde jets, with a strong prograde jet at the equator (superrotation) and generally weaker jets in the off-equatorial region. Although Jupiter and Saturn have similar radii, rotation rates, and atmospheric compositions, their jets differ markedly. Both Jupiter and Saturn have strong prograde jets at the equator, with Saturn's equatorial jet being stronger and wider than Jupiter's. But Jupiter has 15–20 off-equatorial jets, whereas Saturn has only 5–10 wider off-equatorial jets. The speed of Jupiter's prograde off-equatorial jets at the level of the visible clouds is about $20\,\mathrm{m\,s^{-1}}$, with the exception of a stronger prograde jet at 21°N (Porco et al. 2003). The speed of Saturn's prograde off-equatorial jets[1] is around $100\,\mathrm{m\,s^{-1}}$. In both atmospheres, prograde jets are generally stronger and sharper than retrograde jets.

We have previously investigated how prograde equatorial jets and off-equatorial jets form and how the speeds and widths of equatorial jets relate to other flow parameters. In brief, prograde equatorial jets can form by convective generation of Rossby waves, which occurs

Corresponding author address: Junjun Liu, California Institute of Technology, MC 131-24, 1200 E. California Blvd., Pasadena, CA 91125. E-mail: ljj@gps.caltech.edu

[1] The rotation period of Saturn is uncertain to within about 10 min (Gurnett et al. 2007). This implies uncertainties about the jet speeds on Saturn. However, even taking these uncertainties into account, off-equatorial jets on Saturn are stronger than those on Jupiter, with wider interjet spacing.

DOI: 10.1175/JAS-D-13-0391.1

preferentially near the equator because there the Rossby number is larger and convection can drive large-scale divergence that acts as a Rossby wave source (Sardeshmukh and Hoskins 1988). The equatorial Rossby waves transport angular momentum toward their source region and lead to superrotation there (Schneider and Liu 2009; Liu and Schneider 2010). The width of prograde equatorial jets is related to the equatorial Rossby radius (scale of the equatorial waves), and their speed scales approximately with the square of their widths (Liu and Schneider 2011). Thus, prograde equatorial jets can form solely by convection associated with intrinsic heat fluxes emanating from the deep interior. However, such convective heat fluxes do not generally give rise to off-equatorial jets: substantial intrinsic heat fluxes support the formation of off-equatorial jets by reducing static stability and thus increasing baroclinicity, but they are generally neither necessary nor sufficient for off-equatorial jet formation. Instead, off-equatorial jets form by interactions between the mean flow and waves generated by baroclinic instability, associated with differential solar heating (Schneider and Liu 2009; Liu and Schneider 2010).

Eddy fluxes of angular momentum into prograde jets and out of retrograde jets are necessary to maintain jets against any drag on the zonal flow. In Jupiter's and Saturn's upper atmospheres, tracking clouds has revealed that eddies indeed transport angular momentum out of retrograde into prograde jets, thereby converting eddy into mean-flow kinetic energy (Salyk et al. 2006; Del Genio et al. 2007). To close the angular momentum budget, this angular momentum transport by eddies must be balanced by drag on zonal flows, absent any compensating eddy angular momentum transport out of prograde into retrograde jets at depth (theory and observations do not provide a basis for such a compensatory transport). For Jupiter and Saturn, the drag acts on the zonal flows in the deep atmosphere at pressure of order 10^6 bar, where the electrical conductivity of hydrogen (the main constituent of Jupiter and Saturn) is relatively high (Nellis et al. 1996; Liu et al. 2008, 2013). Where the atmosphere is electrically conducting, any flow advects the magnetic field and induces an electric current. The Ohmic dissipation of the induced electric current dissipates kinetic energy of the flow (Liu et al. 2008). In the momentum equations for the flow, this dissipation manifests itself as a magnetohydrodynamic (MHD) drag on the flow that acts through the Lorentz force (Grote and Busse 2001; Liu et al. 2008; Heimpel and Gómez Pérez 2011).

The observations of the angular momentum fluxes in the upper atmospheres of Jupiter and Saturn also indicate that the angular momentum flux convergence and divergence must be concentrated in the upper atmosphere at pressures of at most a few bars or less. If they were to extend more deeply, the total kinetic energy transferred from eddies to the mean flow would, implausibly, exceed the total energy available to drive the flow (Ingersoll et al. 1981; Salyk et al. 2006; Schneider and Liu 2009; Liu and Schneider 2010). This stands in contrast to deep-convection models of giant planet atmospheres, in which the energy transfer from eddies to the mean flow extends over great depth (Kaspi et al. 2009), making it necessary to drive the models with very strong energy fluxes if one wants to reproduce the observed scales of eddies and jets in the upper atmosphere (e.g., Heimpel et al. 2005).

Ideally, one would like to be able to simultaneously resolve the interior deep convection and upper-atmospheric baroclinic eddies in simulations of giant planets, with realistic magnitudes of the driving energy fluxes. Unfortunately, this is not computationally feasible for the foreseeable future, both because the scales of eddies in the upper atmosphere are relatively small compared with the planetary scale (hence the large number of jets) and because adjustment time scales of the deep interior are very long (centuries to millennia), requiring long spinup periods. Instead, we employ a simplified approach, focusing on the upper atmospheres, but linking its dynamics to a representation of the MHD drag that in reality occurs at great depth. The angular momentum balance requires that any net angular momentum flux convergence (divergence) integrated over a surface of constant specific angular momentum in a statistically steady state must be balanced by drag on a prograde (retrograde) zonal flow somewhere on that angular momentum surface (Green 1970; Haynes et al. 1991; Vallis 2006). The ''downward control'' principle stipulates that mean meridional circulations and zonal flows generally extend downward to wherever the drag acts to achieve a closed angular momentum budget (Haynes et al. 1991; O'Gorman and Schneider 2008; Schneider and Liu 2009; Liu and Schneider 2010). For the giant planets, this means that angular momentum flux convergence into a prograde jet must be balanced by drag on a prograde flow on an angular momentum surface that connects the upper-atmosphere jet with the drag region at depth. Because outside a few degrees off the equator, where the Rossby number is small, angular momentum surfaces are cylinders concentric with the planet's spin axis, there exists a region near the equator where these cylinders do not intersect the drag region at depth, and in which, therefore, no drag can balance the angular momentum flux convergence and divergence in the upper troposphere. In our GCM, which simulates a thin atmospheric shell, we mimic this lack of drag near the equator by having a latitude span without drag. Otherwise, we use linear Rayleigh drag at the GCM's bottom boundary to represent the MHD drag that in reality occurs at much greater depth (Schneider

and Liu 2009; Liu and Schneider 2010). We vary the strength of the off-equatorial drag to examine how it affects flow characteristics such as eddy length scales and jet scales.

The effects of drag on geophysical turbulence have been studied extensively using two-dimensional and shallow-water models (Danilov and Gurarie 2002; Smith et al. 2002; Galperin et al. 2006; Scott and Dritschel 2013) and in the quasigeostrophic two-layer model (Thompson and Young 2007). In general, drag removes energy from the system and contributes to halting the inverse cascade (Vallis 2006). If the drag is sufficiently strong, it removes the energy from the system before it is transferred upscale and preferentially into the zonal direction to form zonal jets. Hence, strong drag inhibits the formation of zonal jets through an inverse energy cascade (Danilov and Gurarie 2002). However, zonal jets form with sufficiently weak drag, and the eddy length scales and jet scales generally increase as the drag weakens (Danilov and Gurarie 2002; Smith et al. 2002; Scott and Dritschel 2013). Here we investigate how similar processes that were found to be important in these more idealized models play out in a more realistic (if still idealized) three-dimensional setting.

For Jupiter and Saturn, the strength of the MHD drag depends on the magnitude of the magnetic field, among other factors. There are no direct measurements of the magnetic fields in the planetary interiors. But the measured magnetic field in Jupiter's upper atmosphere is about 20 times stronger than that in Saturn's upper atmosphere (Connerney 1993). Therefore, the magnetic field in Jupiter's interior may also be stronger and produce stronger MHD drag. Our study is in part motivated by wanting to understand to what extent this difference in magnetic field strength and hence in MHD drag can account for differences in the observed upper-atmospheric flow characteristics. With a variant of the GCM we used in previous studies (Schneider and Liu 2009; Liu and Schneider 2010, 2011), we study how and why variations in drag strength lead to flow variations. Section 2 describes the GCM and the simulations we conducted. Section 3 describes how the zonal flows and eddy momentum fluxes vary as the drag coefficient at the lower boundary of the GCM domain is varied. Section 4 analyzes the energy cycle in the simulations, which is important for understanding how mean zonal flows vary with the drag coefficient. Section 5 discusses how dissipation affects turbulence characteristics. Section 6 summarizes the conclusions and discusses their implications for Jupiter and Saturn.

2. Idealized GCM

a. Model description

We use an idealized primitive equation GCM of a dry ideal-gas atmosphere, similar to that described in Schneider and Liu (2009). The GCM uses the spectral transform method in the horizontal (T213 resolution) and finite differences in the vertical (30 uniformly spaced σ levels). Radiative transfer is represented by a gray radiation scheme, with absorption and scattering of solar radiation and absorption and emission of thermal radiation. Diffusively incident equinox insolation is prescribed at the top of the atmosphere. At the lower boundary, a spatially uniform and temporally constant heat flux is imposed to represent the intrinsic planetary heat flux. The model includes a dry convection scheme that relaxes convectively unstable columns to a dry-adiabatic temperature profile. We use parameters relevant to Jupiter (planetary radius, rotation rate, gas constants, etc.) as in Schneider and Liu (2009), except for the drag parameters discussed below. As a slight difference from the simulations in our previous papers, here we use the modified Robert–Asselin filter of Williams (2011) to reduce the numerical errors produced in the leapfrog time-stepping scheme.

b. Rayleigh drag and subgrid-scale dissipation

In Jupiter's and Saturn's atmospheres, the electrical conductivity of hydrogen (the main atmospheric constituent) increases exponentially with depth. Calculations using a semiconductor model with linear band gaps determined by experimental shockwave data (Nellis et al. 1992, 1996) indicated that the electrical conductivity increases exponentially with depth until it reaches about $2 \times 10^5\,\mathrm{S\,m^{-1}}$ at $0.84R_J$ on Jupiter (Jupiter radius R_J) and at $0.63R_S$ on Saturn (Saturn radius R_S), where hydrogen becomes metallic.[2] The interaction of the magnetic field with the flow in the electrically conducting region produces Ohmic dissipation and leads to the MHD drag on the flow (see appendix for more details on the MHD drag and how it relates to our simplified representation).

As a simplified representation of the MHD drag, we impose Rayleigh drag $\mathbf{F}_R$ near the lower boundary of the GCM in the horizontal momentum equations:

$$\mathbf{F}_R = -k(\phi, \sigma)\mathbf{v}, \tag{1}$$

where ϕ is latitude and $\mathbf{v}$ the horizontal velocity. As in Held and Suarez (1994), the drag coefficient $k(\phi, \sigma)$

[2] The electrical conductivity in Jupiter's interior has also been calculated using ab initio simulations (French et al. 2012). Above $0.94R_J$, it agrees well with the calculation based on the semiconductor model with linear band gaps. Below $0.94R_J$, the electrical conductivity determined by ab initio simulations increases more rapidly with depth and reaches $10^6\,\mathrm{S\,m^{-1}}$ at around $0.1R_J$.

decreases linearly in σ from its value $k_0(\phi)$ at the lower boundary ($\sigma = 1$) to zero at $\sigma_b = 0.8$:

$$k(\phi, \sigma) = \frac{1}{\tau_d(\phi)} \max\left(0, \frac{\sigma - \sigma_b}{1 - \sigma_b}\right). \quad (2)$$

Here, $\tau_d(\phi)$ is the drag time scale, which varies with latitude ϕ because the MHD drag affects the flow in the upper atmosphere through mean meridional circulations that are approximately aligned with surfaces of constant planetary angular momentum per unit mass where eddy momentum fluxes and drag are weak. These surfaces are cylinders concentric with the planetary spin axis. Therefore, to represent in the thin atmospheric shell of the GCM domain the MHD drag in the deep interior, we choose $k(\phi, \sigma) = 0$ in the equatorial region with $|\phi| \le \phi_e$, where cylinders concentric with the spin axis do not intersect the electrically conducting region at depth. The equatorial no-drag region in our simulations extends to $\phi_e = 26°$ latitude in each hemisphere, corresponding to drag being significant only below $0.9R_J$ (because arccos 0.9 = 26°), which is consistent with estimates for the depth at which the drag acts on Jupiter (Liu et al. 2013). Outside the no-drag region, the drag time scale is set to a constant τ_0 with respect to latitude [$\tau_d(\phi) = \tau_0$ for $|\phi| > \phi_e$]. See Schneider and Liu (2009), Liu and Schneider (2010), and Liu et al. (2013) for a more detailed justification of the drag parameterization. In this paper, we vary the off-equatorial drag time scale τ_0 over a wide range (from 5 to 1000 d, where 1 d = 86 400 s ≈ 1 Earth day) to investigate the effect of the bottom drag on the off-equatorial jets.

Horizontal hyperdiffusion in the vorticity, divergence, and temperature equations is the only other dissipative process in the GCM, acting at all levels. The hyperdiffusion is represented by an exponential cutoff filter (Smith et al. 2002), with a damping time scale of 2 h at the smallest resolved scale and with no damping for spherical wavenumbers less than 100. The heat generated by the subgrid-scale hyperdiffusion of momentum is not returned to the atmosphere, as is common in atmospheric GCMs, implying that the GCM does not exactly conserve energy. However, the energy loss is small compared with the overall energy input to the atmosphere; it does not significantly influence the energetics of the atmosphere.

c. Simulations

We first spun up a simulation with an off-equatorial drag time scale $\tau_0 = 10$ d at T85 horizontal resolution for 50 000 Earth days. The end state of the T85 simulation was used as initial state of a T213 simulation, which was spun up for an additional 25 000 days, after which a statistically steady state was reached. Simulations with other off-equatorial drag time scales (between 5 and 1000 d) were spun up from the end state of the $\tau_0 = 10$-d simulation for at least 25 000 days. The statistics we show are computed from 500 simulated days sampled 4 times daily in the statistically steady states of the simulations. The only two exceptions are for the kinetic energy spectra (averaged over 2000 d) and for the energy conversion rates in the low-drag simulations (with $\tau_0 = 200$, 500, and 1000 d) (averaged for more than 5000 d). The GCM's time step is 900 s for strong-drag simulations (τ_0 between 5 and 100 d) and 600 s for weak-drag simulations ($\tau_0 = 200$, 500, and 1000 d).

Figure 1 shows how the zonal flows and thermal structures in the simulations change as the off-equatorial drag time scale increases. Like in two-dimensional simulations (Danilov and Gurarie 2002; Smith et al. 2002; Scott and Dritschel 2013), the speed and width of the off-equatorial jets increase as the drag time scale increases (left panels). For $\tau_0 = 5$ d, there are about six prograde jets in each hemisphere, with average speeds of 5–20 m s^{-1} and widths of 2°–5° in the upper troposphere (at the level of the visible clouds on Jupiter, ~0.65 bar). For $\tau_0 = 100$ d, there are about three prograde jets in each hemisphere, with average speeds of 75–80 m s^{-1} and widths of 5°–10°. For $\tau_0 = 1000$ d, there are only two jets remaining in each hemisphere. Their upper-tropospheric speeds reach 120–140 m s^{-1}, and their widths reach 10°–15°. As the drag time scale increases, the interjet spacing also increases, from ~10° for $\tau_0 = 5$ d to ~45° for $\tau_0 = 1000$ d. At the same time, the width and speed of the prograde equatorial jet decrease as the off-equatorial drag time scale increases up to $\tau_0 \approx 1000$ d (the equatorial drag is zero in all simulations). For example, at 0.65 bar, the speed of the equatorial jet decreases from ~80 m s^{-1} for $\tau_0 = 5$ d to ~60 m s^{-1} for $\tau_0 = 100$ d, and then it decreases again to ~40 m s^{-1} for $\tau_0 = 1000$ d. However, the thermal structure of the atmosphere hardly changes as the drag time scale is increased (right panels).

As the drag weakens, the off-equatorial jets strengthen and widen and become more barotropic (James and Gray 1986). As a result, larger meridional pressure variations are required to maintain geostrophic balance at leading order, implying large meridional pressure variations even at the lower boundary because even there jet strengths are still substantial. For $\tau = 5$ d, the surface pressure varies along the lower boundary of the GCM (at a mean pressure of 3 bar) by less than 0.25 bar; however, it varies by more than 1 bar for the simulation with drag time scale of 1000 d. This surface pressure variation leads to substantial deviations of the σ coordinates used in Fig. 1 and subsequent figures from pressure coordinates.

Figure 2 shows that the jets are also evident in instantaneous snapshots of the vorticity field. As the drag time scale increases (drag decreases), the jets form

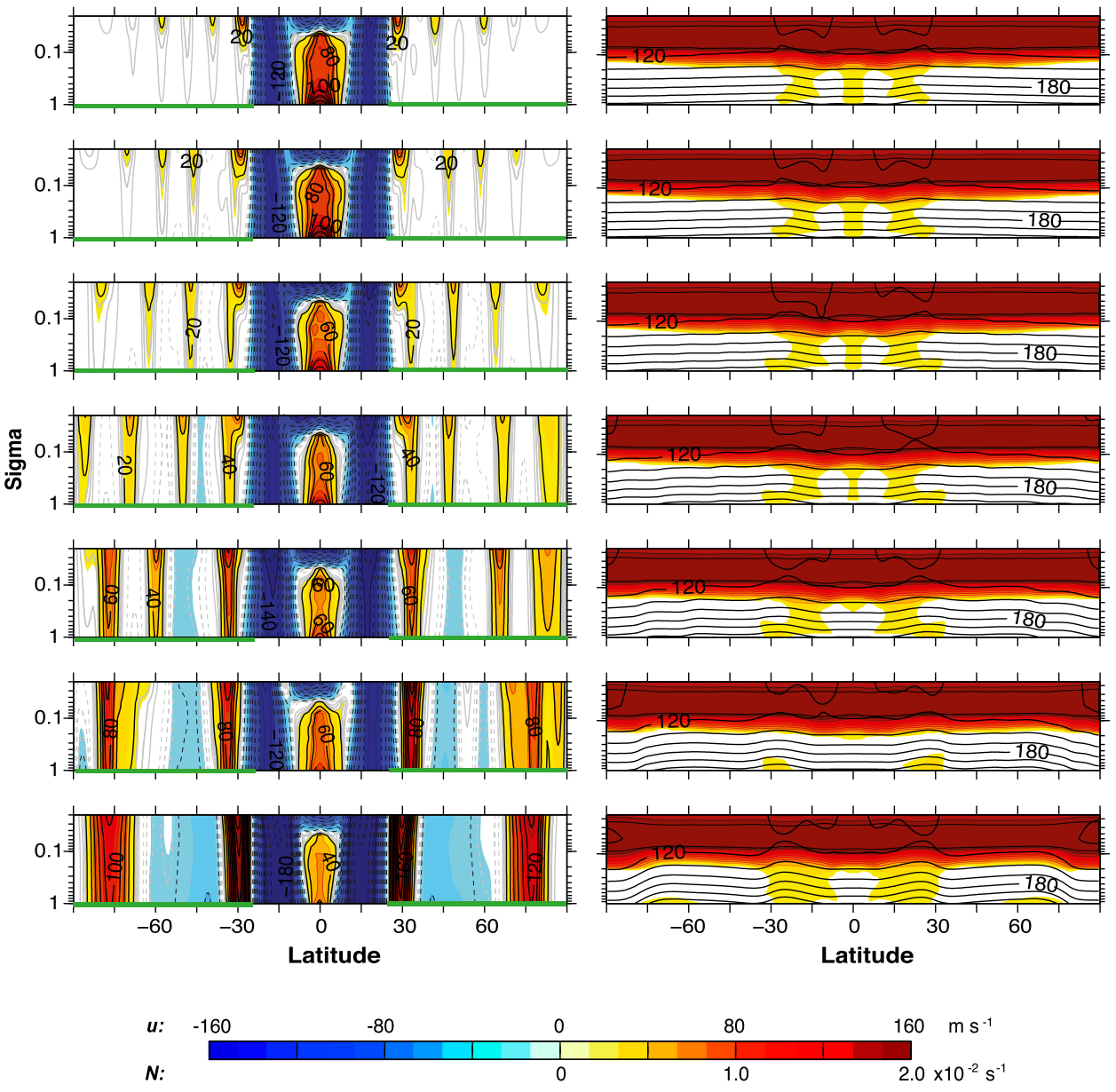

FIG. 1. Flow fields in the latitude–pressure plane in different simulations. (left) Mean zonal velocity $\overline{u}$. Prograde flows are shown in warm colors and with solid contours, and retrograde flows are shown in cold colors and with dashed contours. Gray contours for zonal flow speeds between 5–15 m s^{-1} with a contour interval of 5 m s^{-1}; black contours for zonal flow speeds $\geq$ 20 m s^{-1} with a contour interval of 20 m s^{-1}. The thick green lines at the panel bottoms indicate the region with nonzero drag (poleward of 26°N/S). (right) Temperature (contours with interval of 20 K) and buoyancy frequency N (colors). The off-equatorial Rayleigh drag time scales τ_0 in the simulations increase: (top to bottom) 5, 10, 20, 40, 100, 200, and 1000 d.

larger meanders and coherent vortices become larger and more prevalent on the flanks of the jets. The coherent vortices are advected by the zonal flows and have lifespans similar to the drag time scale, suggesting that frictional spindown limits their lifetime.

To understand these changes of the flow as the drag time scale changes, we turn to the angular momentum and energy budgets of the circulations.

3. Angular momentum budget

The angular momentum budget constrains the zonal surface winds on Earth (e.g., Green 1970) and, more generally, it constrains the zonal flow in any region of drag even in the absence of a solid surface, as on the giant planets. To see this, consider the angular momentum budget for a general, potentially deep atmosphere in the

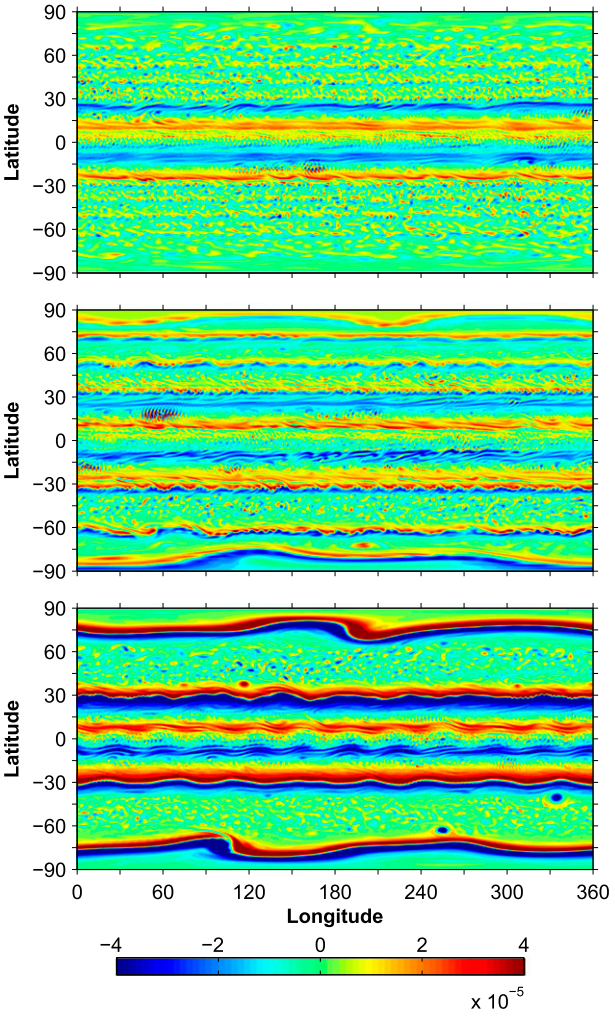

FIG. 2. Vorticity (s^{-1}) at 0.65 bar in the longitude–latitude plane in three different simulations. The off-equatorial Rayleigh drag time scale increases: (top to bottom) 10, 100, and 1000 d.

limit of small Rossby number $\mathrm{Ro} = U/(2\Omega L_\perp)$, with zonal velocity scale U, planetary angular velocity Ω, and length scale of flow variations in the cylindrically radial direction $L_\perp$ ($L_\perp = L\sin\phi$; this is the projection of a meridional length scale L at latitude ϕ onto the equatorial plane). As discussed in Schneider and Liu (2009) and Liu and Schneider (2010), in this limit, which is adequate for the off-equatorial jets on Jupiter and Saturn, the angular momentum balance in a statistically steady state becomes

$$\overline{\mathbf{u}}^* \cdot \nabla M_\Omega \approx r_\perp \overline{F}^* - S, \tag{3}$$

where $M_\Omega = \Omega r_\perp^2$ is the planetary component of the angular momentum about the planet's spin axis, $r_\perp$ being the cylindrical distance to the spin axis. In the thin-shell approximation, the left-hand side becomes $\overline{\mathbf{u}}^* \cdot \nabla M_\Omega = -f\overline{v}^* r_\perp$ (with Coriolis parameter $f = 2\Omega\sin\phi$); it represents the Coriolis torque per unit mass (cf. Kaspi et al. 2009). On the right-hand side, there is the zonal drag force F per unit mass, and the divergence of the eddy flux of angular momentum

$$S = \frac{1}{\overline{\rho}} \mathrm{div}(\overline{\rho}\,\overline{\mathbf{u}'u'}^* r_\perp), \tag{4}$$

where $\mathbf{u}$ is the three-dimensional velocity with zonal component u and meridional component v. The overbar $\overline{(\cdot)}$ denotes a temporal and zonal mean at constant $r_\perp$, $\overline{(\cdot)}^* = \overline{(\rho\,\cdot)}/\overline{\rho}$ denotes the corresponding density-weighted mean, and primes $(\cdot)' = (\cdot) - \overline{(\cdot)}^*$ denote deviations from the latter.[3]

If we weight by density and integrate the steady-state angular momentum balance (3) along surfaces of constant planetary angular momentum M_Ω (a vertical integral in thin-shell approximation, or an integral along the direction of the spin axis in a deep atmosphere), we obtain

$$\langle \overline{\rho} S \rangle_\Omega = r_\perp \langle \overline{\rho}\,\overline{F}^* \rangle_\Omega, \tag{5}$$

where $\langle\cdot\rangle_\Omega$ denotes an integral over M_Ω surfaces (Haynes et al. 1991; Schneider and Liu 2009; Liu and Schneider 2010). The left-hand side of (3) integrates to zero because there can be no net mass flux across an M_Ω surface in a statistically steady state. Therefore, any net eddy angular momentum flux convergence or divergence on an M_Ω surface must be balanced by a zonal drag force on the same M_Ω surface. Since the Rayleigh drag in the simulations is only imposed near the bottom of the domain ($\sigma > 0.8$), we have

$$\langle \overline{\rho} S \rangle_\Omega = r_\perp \langle \overline{\rho}\,\overline{F}^* \rangle_\Omega \propto -r_\perp H_d \overline{\rho}_d \overline{u}_d^* / \tau_d, \tag{6}$$

where the subscript d denotes quantities in the drag layer and H_d is a measure of the thickness of the drag layer. Therefore, everything else being unchanged, the drag-layer zonal flow $\overline{u}_d^*$ is proportional to the vertically integrated eddy flux of angular momentum $\langle \overline{\rho} S \rangle_\Omega$ and the drag time scale τ_d. The drag time scale associated with the Lorentz force scales like $\tau_d \sim \rho_d/\sigma_d B_d^2$, where σ_d is the magnitude of the electrical conductivity in the drag layer and B_d is the magnitude of the magnetic field in the drag layer (see appendix). Thus, the angular momentum balance must satisfy roughly

$$\langle \overline{\rho} S \rangle_\Omega \sim -r_\perp H_d \overline{u}_d^* \sigma_d B_d^2; \tag{7}$$

[3] In actual calculations of these quantities from GCM simulations, we use the analogous surface pressure-weighted averages along the model's σ coordinate surfaces; see Schneider and Walker (2006).

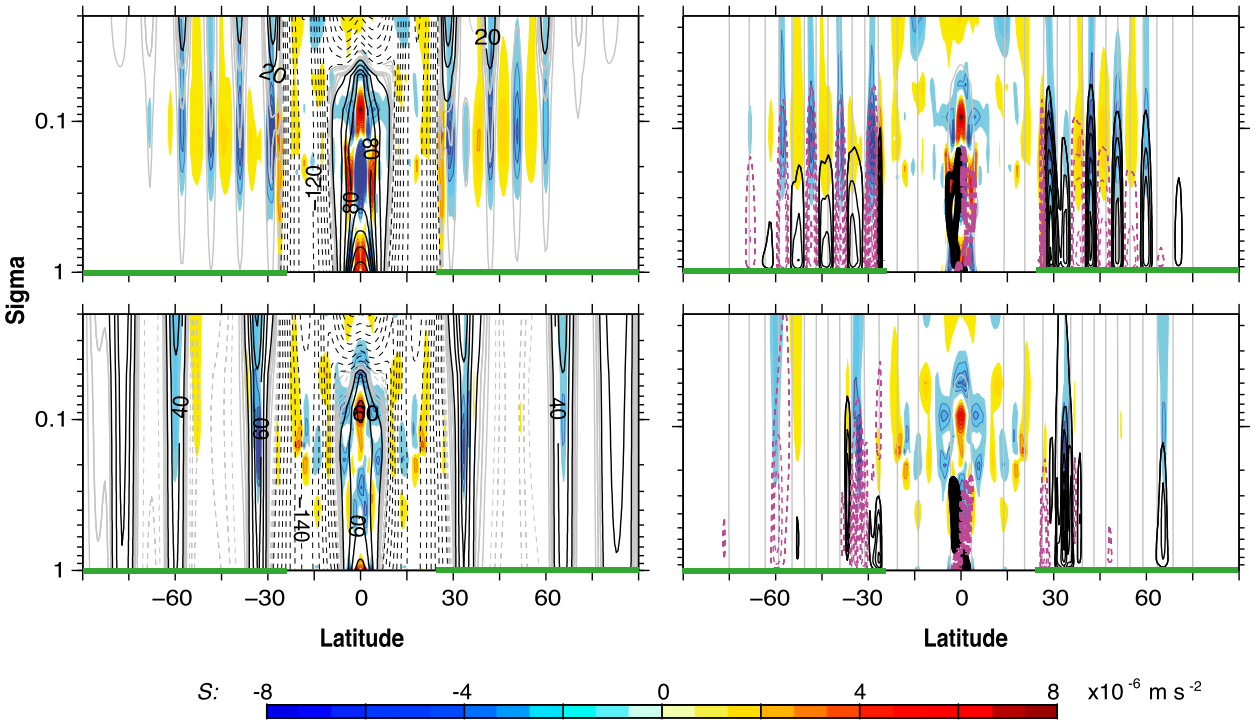

FIG. 3. Mean zonal velocity, eddy momentum flux divergence, and mass flux streamfunction in the latitude–pressure plane in two simulations. (left) Mean zonal velocity $\overline{u}$ (contours) and divergence $\overline{\rho}^{-1}\mathrm{div}(\overline{\rho}\,\overline{u'v'}^{*}r_{\perp})$ of meridional eddy angular momentum flux (colors). Contour intervals for zonal velocities as in Fig. 1. (right) Mass flux streamfunction (contours) and meridional eddy momentum flux divergence (colors, warm for divergence and cold for convergence). The contouring for the mass flux streamfunction is $2.5 \times 10^{8}\,\mathrm{kg\,s^{-1}}$ poleward of 26°N/S and $5 \times 10^{9}\,\mathrm{kg\,s^{-1}}$ equatorward of 26°N/S. The thick green lines at the panel bottoms mark the regions with nonzero drag. The off-equatorial Rayleigh drag time scales τ_0 are (top) 5 and (bottom) 10 d.

hence, for a given net eddy angular momentum flux convergence or divergence on an M_Ω surface, the drag-layer zonal flow $\overline{u}_d^*$ scales inversely with the square of the magnetic field strength B_d^2.

In Jupiter's and Saturn's atmospheres, the divergence and convergence of eddy fluxes of angular momentum appears to be concentrated in the upper troposphere, as it is on Earth.[4] If it were to extend much more deeply, the associated conversion rate from eddy to mean-flow kinetic energy (Salyk et al. 2006) would exceed the total energy available to drive the flow, which is implausible (Schneider and Liu 2009; Liu and Schneider 2010). Similarly, in our simulations, the divergence and convergence of eddy angular momentum fluxes in the off-equatorial region are concentrated in the upper troposphere above ~1 bar. Variation of the drag time scale near the bottom of the simulation domain does not strongly influence the tropospheric thermal structure or the magnitude of the angular momentum fluxes aloft (Figs. 1 and 3), which are predominantly controlled by the thermal structure (Schneider and Walker 2008). Thus, although the drag time scale varies over two orders of magnitude, the eddy angular momentum flux divergence/convergence varies only by a factor of ~4 across our simulations (Fig. 4b). But the zonal flow speed varies by more than a factor of ~40 across the simulations, both in the drag layer and aloft (Fig. 4a). Therefore, according to (6) and in a first approximation, the drag-layer zonal flow strengthens with the drag time scale, though not linearly but modulated by changes in eddy angular momentum fluxes in particular at the strong-drag end. At the extreme weak-drag end (not reached in our simulations),

[4] This does not necessarily mean that the generation of the waves responsible for the angular momentum flux is concentrated in the upper troposphere (cf. Del Genio and Barbara 2012). In Earth's atmosphere, baroclinic waves are generated near the surface and propagate upward before they propagate meridionally, giving rise to the observed angular momentum fluxes (Simmons and Hoskins 1976, 1977). Similarly, wave generation and eddy angular momentum fluxes may not be collocated in the vertical on giant planets. Off-equatorial Rossby waves are more likely generated in the lower troposphere, where the intrinsic heat fluxes render the stratification nearly statically neutral so that the baroclinicity is large. From there they may propagate upward and give rise to the eddy fluxes of angular momentum that are observed to peak below the tropopause (Salyk et al. 2006; Del Genio et al. 2007).

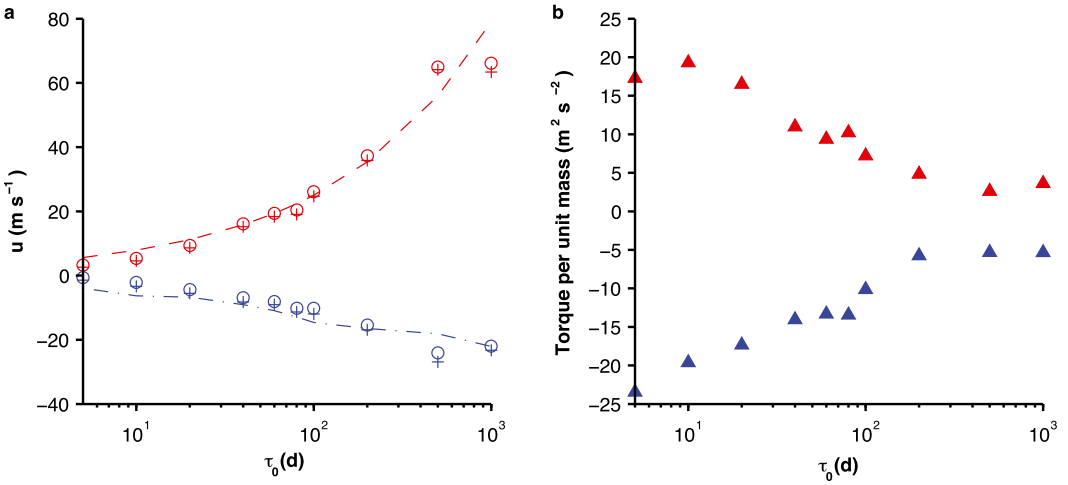

FIG. 4. (a) Mean zonal velocity (red for prograde and blue for retrograde winds) at 0.65 (circles) and 2.0 bar (plus signs). The mean zonal velocities are averaged in the off-equatorial region poleward of 26°N/S, taking separate averages for prograde ($u > 0$) and retrograde ($u < 0$) flows. The red dashed lines show a $\tau_0^{1/2}$ fit to the drag-layer zonal velocities. The blue dashed–dotted lines show the minimum retrograde flow ($u < 0$ with maximum $|u|$) constrained by the sufficient condition for barotropic stability $u_{\min} = -K_b\beta\langle L_e\rangle^2/2$, where β is calculated at 55°N and $\langle L_e\rangle$ is the meridionally averaged energy-containing eddy length scale averaged in the off-equatorial region poleward of 26°N/S, and $K_b = 1/250$ is a scaling factor. (b) Vertically averaged eddy angular momentum flux convergence (blue triangles) and divergence (red triangles) in the off-equatorial region poleward of 26°N/S, taking separate averages for convergence and divergence.

this relation is expected to break down, as the strengthening zonal flow will shear eddies apart and inhibit the eddy transport of angular momentum and other properties: the "barotropic governor" effect (James and Gray 1986). This would eventually limit the strengthening of the zonal flows.

The strength of the jets in the upper troposphere is determined by the strength of the zonal flow in the drag layer and the (thermal wind) shear between there and the upper troposphere. Since the thermal structure of the off-equatorial troposphere to first order is unaffected by the drag time scale, the off-equatorial thermal wind shear remains essentially unchanged as the drag time scale is varied. Therefore, the jets in the upper troposphere strengthen roughly in proportion to the zonal flow in the drag layer, which increases with the drag time scale (Fig. 4a).

To understand the zonal flow changes in more detail, we turn to the energy budget.

4. Energy budget

Unlike Earth's atmosphere, the atmospheres of Jupiter and Saturn are heated substantially not only by differential solar radiation but also by intrinsic heat fluxes emanating from the deep interior. The absorbed solar flux amounts to 8.1 W m^{-2} for Jupiter and 2.7 W m^{-2} for Saturn in the global mean; the intrinsic heat fluxes are comparable: 5.7 W m^{-2} for Jupiter and 2.0 W m^{-2} for Saturn (Guillot 2005). Our simulations here are consistent with the observed energetics for Jupiter. We investigate how the thermodynamic efficiency of the atmosphere varies with drag time scale.

Because of the strong intrinsic heat fluxes, Jupiter and Saturn's atmospheres are close to statically neutral below the tropopause, as shown in measurements by the Galileo probe as it descended into Jupiter (Magalhães et al. 2002), as well as in our simulations (Fig. 1). Away from the equator and below the upper tropospheres, the rapid planetary rotation and the weak viscosity constrain convective motions to homogenize entropy along angular momentum surfaces: approximately cylinders parallel to the spin axis in deep atmospheres, or approximately vertical lines in the thin-shell approximation (Liu et al. 2013). The available potential energy introduced by Lorenz (1955) is based on redistributing mass horizontally within isentropic layers; it is not well defined where the stratification is neutral. Hence, we consider the total potential energy instead (Peixoto and Oort 1992).

Defining the total potential energy P and kinetic energy K as

$$P = \int_M c_p T \, dm,$$
$$K = \int_M \frac{\mathbf{u}\cdot\mathbf{u}}{2} dm, \tag{8}$$

where $\int_M$ is the mass-weighted global integral and c_p is the specific heat per unit volume, the energy cycle can be summarized as

$$\frac{\partial P}{\partial t} = G(P) - C(P,K),$$
$$\frac{\partial K}{\partial t} = C(P,K) - D(K). \quad (9)$$

Diabatic heating generates potential energy P at a rate $G(P)$, which is then converted baroclinically to kinetic energy K at rate $C(P, K)$, which in turn is dissipated into heat at a rate $D(K)$ (e.g., Peixoto and Oort 1992). In a statistically steady state, $G(P)$, $C(P, K)$, and $D(K)$ balance each other.

Jupiter's and Saturn's atmospheres are not bounded by solid surfaces, and there are no clear boundaries between the upper atmospheres and the deep interiors. Hydrogen, the main constituent of Jupiter and Saturn, behaves significantly differently from an ideal gas in the planetary interiors (Guillot et al. 2004). However, within our GCM domain in the upper atmosphere, the atmosphere can be approximated as an ideal gas. As the GCM domain captures the region where the vast majority of the solar radiation is absorbed, one may hope that inferences about the energy budget from this limited domain are relevant for the planet more broadly, although we do not explicitly capture the deeper dynamics. Hence, we use the thin-shell approximation with a dry ideal-gas equation of state, as implemented in the GCM. The generation rate of potential energy $G(P)$ is then defined as

$$G(P) = \int_M Q\, dm, \quad (10)$$

where Q is the total diabatic heating rate (temperature tendency) from radiative energy fluxes, intrinsic heat fluxes, and frictional heating. Solar radiative heating, longwave radiative cooling, and the intrinsic heat flux dominate $G(P)$, but the frictional heating from the Rayleigh drag also accounts for 10%–20% of $G(P)$. The baroclinic conversion rate $C(P, K)$ from potential energy to kinetic energy is defined as

$$C(P,K) = -\int_M \omega\alpha\, dm, \quad (11)$$

where α is the specific volume and $\omega = dp/dt$ is the vertical velocity in pressure coordinates.

How does the energy cycle vary with the drag time scale? Generally, as it must in a statistically steady state, the potential energy generation $G(P)$ balances the baroclinic energy conversion $C(P, K)$. Both terms remain roughly constant as the drag time scale is varied (Fig. 5). However, for the weak-drag simulations (τ_0 = 200, 500, and 1000 d), the baroclinic energy conversion rate $C(P, K)$ and the generation rate of potential energy $G(P)$ exhibit low-frequency variations over time scales of 500–1000 d. The conversion rates shown in Fig. 5 are averages for more than 5000 days to reduce the impact of low-frequency variations. The thermodynamic efficiency of the atmosphere η may be defined as the ratio of baroclinic energy conversion $C(P, K)$ [or dissipation $D(K)$] to the total energy input. For Jupiter, the total energy input from absorption of solar radiation and intrinsic heat fluxes is 14.8 W m^{-2}. Taking the conversion rate from our simulations, $C(P, K) \approx 0.4$ W m^{-2}, the implied efficiency is ~2.7%. This is of similar magnitude as, albeit larger than, the thermodynamic efficiency of Earth's atmosphere, which is ~1% (Peixoto and Oort 1992).[5] It indicates that Jupiter's atmosphere is likely more efficient, and this efficiency is not sensitive to drag parameters.

As the drag time scale varies, the dissipation rate from Rayleigh drag at the bottom of the GCM domain, $D_R(K)$, also remains constant, with a magnitude of ~0.08 W m^{-2}. However, this dissipation rate is too small to balance the baroclinic energy conversion rate $C(P, K)$

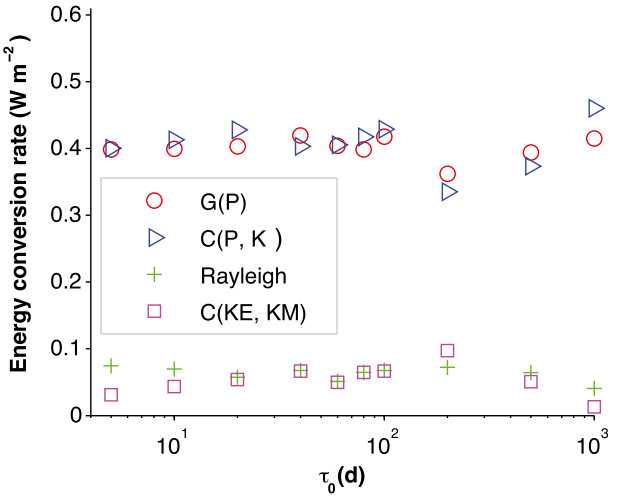

FIG. 5. Rates of potential energy generation $G(P)$ (red circles), baroclinic energy conversion $C(P, K)$ (blue triangles), energy dissipation by Rayleigh drag $D_R(K)$ (green plus signs), and barotropic conversion from eddy to mean kinetic energy $C(K_E, K_M)$ (magenta squares), all as a function of the drag time scale τ_0.

[5] We also calculated the thermodynamic efficiency with an idealized GCM using standard parameters for Earth's atmosphere. The derived efficiency is about 1.2%, which is consistent with the estimated efficiency from the observations (Peixoto and Oort 1992).

and the generation rate of potential energy $G(P)$. The remaining dissipation of kinetic energy in the GCM is provided by subgrid-scale (SGS) dissipation associated with the exponential filter. (We have verified by explicit calculation for some simulations that the SGS filter indeed provides the missing dissipation and the energy cycle closes with its inclusion.) SGS dissipation provides a large fraction (70%–80%) of the total dissipation because it effectively damps grid-scale motions driven by the parameterized convection in our GCM. It is possible that also on Jupiter and Saturn, dissipation within and around convective plumes provides a large fraction of the total kinetic energy dissipation, as appears to be the case in Earth's tropics (Pauluis and Dias 2012).

The Rayleigh drag primarily acts on the mean (primarily zonal) velocities. As the SGS dissipation is very scale selective and leaves the large-scale mean flow essentially unaffected, almost all dissipation of the kinetic energy of the mean flow occurs in the bottom drag layer. As a result, the dissipation rate by the Rayleigh drag approximately balances the barotropic energy conversion rate from eddy kinetic energy to mean-flow kinetic energy, given by (Peixoto and Oort 1992)

$$C(K_E, K_M) \approx \int_M \overline{u'v'}^* \cos\phi \frac{\partial(\overline{u}^* \cos^{-1}\phi)}{a\partial\phi} dm. \quad (12)$$

The barotropic conversion is dominated by the meridional eddy flux of angular momentum; other terms omitted in (12), involving vertical momentum fluxes and mean meridional velocities, are $O(\mathrm{Ro})$ smaller. Thus, the conversion of eddy to mean-flow kinetic energy by eddy angular momentum fluxes that converge in prograde jets and diverge in retrograde jets is balanced by dissipation of mean-flow kinetic energy. The dissipation of mean-flow kinetic energy in our GCM occurs almost entirely in the bottom drag layer, notwithstanding that much of the kinetic energy of small-scale fluctuations is dissipated by the SGS filter. Like the dissipation associated with the Rayleigh drag at the bottom, the conversion rate of eddy to mean-flow kinetic energy is remarkably insensitive to the drag time scale—more insensitive than the eddy angular momentum fluxes themselves (cf. Fig. 4b).

The near constancy of the conversion of eddy to mean-flow kinetic energy and of the dissipation of mean-flow kinetic energy in the bottom drag layer allows us to refine the statement of how the mean zonal flow depends on the drag time scale. Given that the mean-flow kinetic energy dissipation scales like $\tau_d(\overline{u}^*)^2$, and this is nearly constant as the drag time scale is varied, it follows that $\overline{u}^* \propto \tau_0^{1/2}$ away from the equator. Figure 4a shows that the speeds of the prograde jets in our simulations indeed scale with the square root of the drag time scale. Retrograde jets appear to be limited by barotropic instability and hence are weaker (Rhines 1994). They scale with the minimum retrograde velocity $u < 0$ that is achievable without violating the necessary condition for barotropic instability, $u_{\min} \approx -K_b\beta\langle L_e\rangle^2/2$ (Fig. 4a), where K_b is a constant scaling factor and $\langle L_e\rangle$ is the meridionally averaged energy-containing eddy length scale in the extratropics (see section 5d).

It remains an open question, however, why the energy conversion rates and the thermodynamic efficiency of the simulated atmospheres remain constant as the drag time scale varies. While one would not expect strong variations of the conversion terms as they primarily depend on the thermal structure in the upper atmosphere, it is curious that relatively slight variations in the eddy angular momentum fluxes and in the mean zonal flow in the upper troposphere conspire to compensate each other in just such a way as to leave the barotropic energy conversion nearly constant.

Energy conversion rates and thermodynamic efficiencies much greater than those in our simulations have been inferred for Jupiter (Salyk et al. 2006). However, our simulations are consistent with the observations from which these higher efficiencies have been inferred. The local conversion rate from eddy to mean-flow kinetic energy [integrand in (12)] is concentrated on the flanks of the prograde jets (Fig. 6). At the cloud level (~0.65 bar), the local conversion rate per unit mass in our simulation reaches $10^{-4}\,\mathrm{W\,kg^{-1}}$, which is similar to the estimated values from cloud tracking in Jupiter's extratropics (Salyk et al. 2006). But in the simulations, the local conversion rate exhibits a baroclinic vertical structure: it is primarily confined to above 1 bar and has much weaker magnitude beneath (Fig. 6). The vertical structure of the conversion rate in Jupiter's atmosphere is unknown. To estimate the global conversion rate, the depth of the atmospheric layer involved in the conversion must be assumed. Assuming that the barotropic conversions extend over a layer 2.5 bar thick (Ingersoll et al. 1981), Salyk et al. (2006) inferred global barotropic conversion rates of 0.7–1.2 $\mathrm{W\,m^{-2}}$—about one order of magnitude larger than in our simulations. This apparent discrepancy arises because in our simulations (Fig. 6), the actual conversion rates from eddy to mean-flow kinetic energy are confined to a much thinner upper-tropospheric layer than was previously assumed. The same may be true for Jupiter.

5. Turbulence characteristics

The bottom drag also affects a variety of turbulence characteristics, such as eddy kinetic energies and eddy length scales.

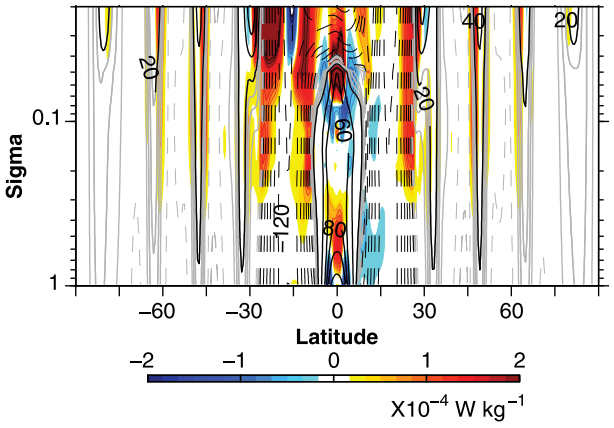

FIG. 6. Local conversion rate from eddy to mean-flow kinetic energy (colors) and zonal wind (contours). Warm colors indicate conversion of kinetic energy from eddies to the mean flow and cool colors represent the converse. The zonal wind contours are as in Fig. 1. The off-equatorial Rayleigh drag time scales τ_0 is 20 d.

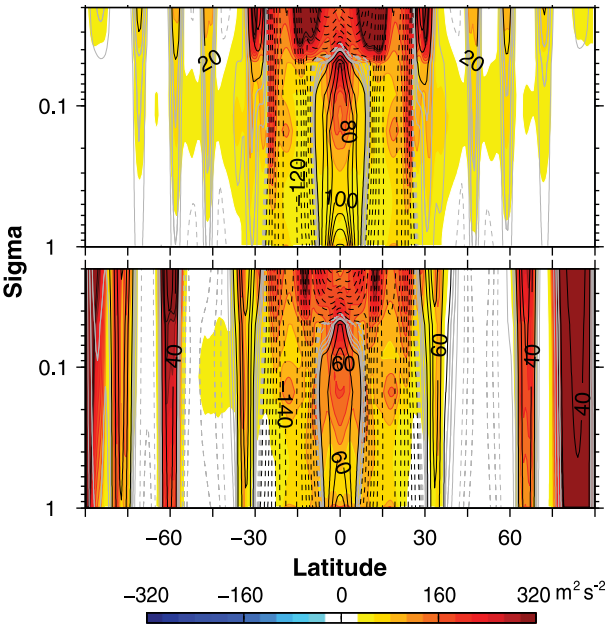

FIG. 7. Eddy kinetic energy per unit area (color contours) and zonal wind (black contours, with intervals as in Fig. 1). The off-equatorial Rayleigh drag time scales τ_0 are (top) 10 and (bottom) 100 d.

a. *Eddy kinetic energy*

The eddy kinetic energy (EKE) is defined as

$$\mathrm{EKE} = \frac{\overline{u'^2}^* + \overline{v'^2}^*}{2}. \tag{13}$$

In the extratropics, EKE is maximal in the jet cores, with much of it associated with the meandering of the zonal jets. Between the jets, EKE exhibits a baroclinic structure and peaks in the layers with significant eddy momentum fluxes (Fig. 7).

The EKE can be decomposed into a barotropic component (EKE of the vertically averaged flow) and a baroclinic component (EKE of the vertically sheared flow). The partitioning between the barotropic EKE and the baroclinic EKE indicates to what degree an inverse cascade of eddy energy from smaller to larger scales exists: if there is an inverse cascade beyond the scale of the linearly most unstable waves, the barotropic EKE exceeds the baroclinic EKE, and their ratio increases with the extent of the inverse cascade (Held and Larichev 1996). In our Jupiter simulations, the barotropic EKE generally exceeds the baroclinic EKE (Fig. 8). As the drag time scale increases, the barotropic EKE increases, while the baroclinic EKE remains largely unchanged. This suggests an inverse cascade that increases in extent as the bottom drag weakens. (In Fig. 8 and subsequent figures showing integrated turbulent characteristics, the results vary with the integration region, here chosen to be the region poleward of 26°N/S; however, these variations do not significantly influence the general results.)

b. *Zonal spectra of eddy velocity variance*

The bottom drag also affects the zonal spectra of eddy velocity variance. Figure 9 shows the latitudinal distribution of the vertically averaged zonal spectra of zonal eddy velocity variance $\overline{u'^2}^*$ and meridional eddy velocity variance $\overline{v'^2}^*$, both as a function of zonal wavelength for different off-equatorial drag time scales. In the equatorial region, the spectra are not substantially influenced by the off-equatorial drag time scale. Both the zonal eddy velocity variance $\overline{u'^2}^*$ and the meridional eddy velocity variance $\overline{v'^2}^*$ exhibit large power over a broad range of long zonal wavelengths ($l \gtrsim 5 \times 10^4$ km). This is consistent with Rossby waves generated by convection organizing into large wave packets in the equatorial region (Schneider and Liu 2009). In the off-equatorial region, the zonal eddy velocity variance $\overline{u'^2}^*$ and the meridional eddy velocity variance $\overline{v'^2}^*$ increase as the drag time scale increases. For weak drag, the meridional eddy velocity variance is comparable with the zonal eddy velocity variance, which implies that the eddy statistics become more isentropic and are less influenced by the zonal jets themselves (Boer and Shepherd 1983). At the boundaries between the extratropical constant drag region and the equatorial no-drag region (26°N/S), the meridional velocity variance exhibits local maxima, which are associated with the strong retrograde zonal jets that flank the equatorial superrotating jet. As the drag time scale and the extratropical baroclinic Rossby

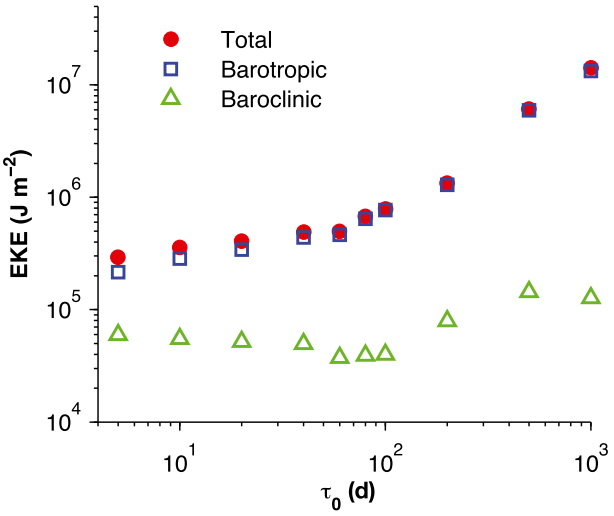

FIG. 8. Eddy kinetic energy per unit area integrated in the region poleward of 26°N/S as a function of drag time scale: total EKE (red circles, filled), barotropic EKE (blue squares), and baroclinic EKE (green triangles).

wave activity increase, the maxima become more prominent, indicating stronger eddy angular momentum transport from midlatitudes into the equatorial region.

Taking sections at fixed latitude through the zonal spectra (Fig. 9), we obtain the zonal spectra of eddy velocity variance in different latitude bands (Fig. 10). In the equatorial region, the zonal spectra of the eddy velocity variance decay slowly with zonal wavenumber m following an approximately $m^{-5/3}$ power law. The spectra have a distinct peak at large wavenumbers ($m \sim 100$), consistent with convective generation of eddy energy at those scales and SGS damping at smaller scales. The spectra are consistent with an inverse cascade of eddy energy from the convective generation scale to larger scales. In midlatitudes, the zonal spectra decay more rapidly with m, following an approximately m^{-3} power law. Notably, there is no distinct peak at large wavenumbers as there is in the equatorial region, consistent with baroclinic generation of eddy energy at larger scales (Schneider and Liu 2009; Liu and Schneider 2010). There is no clear evidence for an inverse energy cascade in midlatitudes. In control simulations without an intrinsic heat flux prescribed at the bottom boundary, the atmosphere is stably stratified in the mean (Schneider and Liu 2009). In that case, the zonal spectra in both the equatorial region and in midlatitudes decay rapidly with m, following an approximately m^{-3} power law. This indicates that convection triggers an inverse cascade in the equatorial region in simulations including intrinsic heat fluxes.

c. *Global barotropic eddy kinetic energy (EKE) spectra*

Further evidence for the presence or absence of an inverse energy cascade comes from the global barotropic EKE spectra as a function of total spherical wavenumber n (Fig. 11). In the spectra, the zonal-mean component ($m = 0$), associated with the jets, is excluded. In the simulations with weaker bottom drag ($\tau_0 \gtrsim 20$ d), the barotropic EKE spectra show an approximate n^{-3} power law dependence on the spherical wavenumber n (Fig. 11b). In the simulations with stronger bottom drag ($\tau_0 \lesssim 10$ d), the barotropic EKE spectra show an approximate $n^{-5/3}$ power law (Fig. 11a). This flatter spectrum in the simulations is consistent with the inertial range in an inverse energy cascade. In the control simulations without intrinsic heat fluxes but with strong drag, the barotropic EKE spectra closely follow an n^{-3} power law. This supports the hypothesis that convection triggers an inverse cascade confined to the equatorial region and causes the flatter EKE spectra globally. Moreover, in all simulations, the nonlinear spectral fluxes of total kinetic energy exhibit an upscale transfer of kinetic energy over a range of wavenumbers between $n \sim 10$ and 100, but this transfer is dominated by eddy–mean flow interactions. The kinetic energy transfer by eddy–eddy interactions, which are considered essential for an inverse cascade, is much weaker (Figs. 11c,d). Thus, eddy–mean flow interactions are more important than eddy–eddy interactions in transferring energy from smaller to larger scales.

The flattening of the global barotropic EKE spectra in the simulations with stronger drag indeed appears to be due to the different characteristics of the turbulent spectra in the equatorial and in the off-equatorial regions. The global barotropic EKE spectra are combinations of the spectra from both regions. Generally, the zonal spectra of eddy velocity variance decay more slowly with zonal wavenumber in the equatorial region than in midlatitudes (Fig. 10). In the simulations with strong drag, the EKE in the off-equatorial region is limited by the drag and hence is relatively small. The global EKE is dominated by the EKE in the equatorial region, and the global EKE spectra show more characteristics of the equatorial region, following an $n^{-5/3}$ power law globally. In the simulations with weak drag, the EKE in the off-equatorial region is larger than that in the equatorial region. Thus, the spectra of the EKE show more characteristics of the spectra in the off-equatorial region and follow an n^{-3} power law.

d. *Kinetic energy of the zonal-mean flows and the zonal kinetic energy spectra*

Across the simulations, the kinetic energy of the zonal-mean flows increases from 10^7 J m^{-2} at $\tau_d = 5$ d to

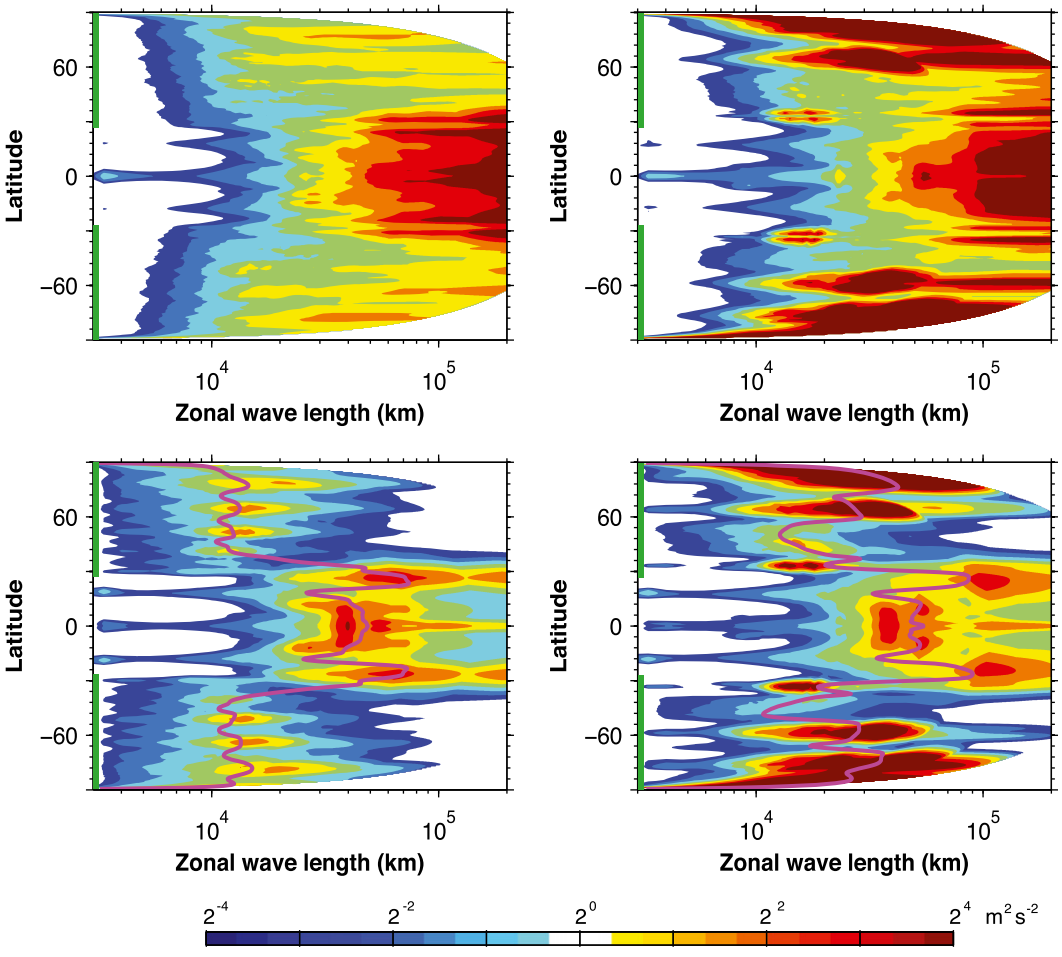

FIG. 9. Mass-weighted vertical mean of zonal spectra of eddy velocity variance: (top) zonal velocity variance $\overline{u'^2}^*$; (bottom) meridional velocity variance $\overline{v'^2}^*$. The velocity variance contouring is logarithmic. The magenta lines in the bottom panels mark the energy-containing zonal wavenumber $m_e(\phi)$, defined as the first negative moment of the zonal spectrum of the meridional eddy velocity variance. (left) The simulation with strong bottom drag (τ_0 = 10 d); (right) the simulation with weak bottom drag (τ_0 = 100 d). The thick green lines on the panels' left axes mark the regions with nonzero drag.

$10^8\,\mathrm{J\,m^{-2}}$ at τ_d = 1000 d, which is much larger than the eddy kinetic energy. The zonal kinetic energy (ZKE) spectrum closely follows an n^{-5} power law (Fig. 12), which is the spectrum of large Rossby waves (Rhines 1975). This indicates that the simulations are close to the zonostrophic regime that is also observed on Jupiter (Galperin et al. 2001, 2014).

e. *Energy-containing eddy length scale*

Given the vertically averaged zonal spectrum of the meridional eddy velocity variance $E_v(m, \phi)$ shown in Fig. 9, we define the energy-containing zonal wavenumber m_e as the first negative moment

$$m_e(\phi) = \left[\frac{\sum_{m\geq 1} m^{-1} E_v(m,\phi)}{\sum_{m\geq 1} E_v(m,\phi)} \right]^{-1}. \tag{14}$$

In this way, the energy-containing eddy length scale L_e becomes the integral scale (e.g., Rhines 1975) given by

$$L_e(\phi) = \frac{2\pi a \cos\phi}{m_e}. \tag{15}$$

This integral definition of the energy-containing eddy length gives a robust estimate of the maximum of the meridional eddy variance (Fig. 9). The eddy length scales in the equatorial region are about 2–3 times larger than those in the off-equatorial region (Fig. 9). In the equatorial region, the eddy length scales do not vary significantly with off-equatorial drag time scale. In the off-equatorial region, the energy-containing length scale does not vary strongly with latitude but increases with drag time scale (Fig. 13). For τ_0 = 10 d, the

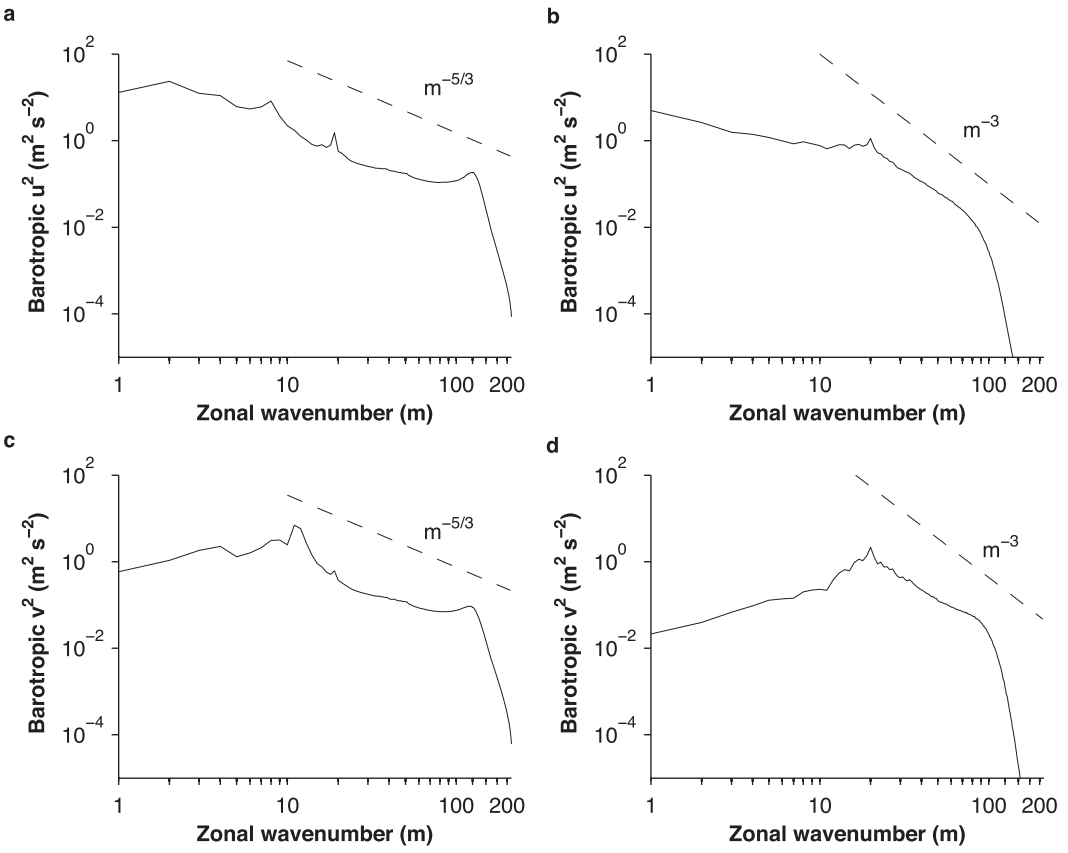

FIG. 10. Zonal spectra of eddy velocity variance in different latitude bands for the simulation with $\tau_0 = 100$ d. (a),(b) Zonal velocity variance $\overline{u'^2}^*$. (c),(d) Meridional velocity variance $\overline{v'^2}^*$. The spectra for (left) the equatorial region (5°S–5°N) and (right) for midlatitudes (35°–45°N).

meridionally averaged eddy length scale $\langle L_e \rangle$ is around 20 000 km. For $\tau_0 = 100$ d, $\langle L_e \rangle$ increases to around 30 000 km.

f. Rhines scale

The energy-containing eddy length scale is well approximated by the Rhines scale L_β (Rhines 1975, 1994)—the scale at which a barotropic Rossby wave frequency (determined by the meridional gradient β of the Coriolis parameter f) becomes comparable to an eddy turnover time. In terms of the barotropic eddy kinetic energy $\mathrm{EKE_{bt}}$, the Rhines scale can be expressed as

$$L_\beta = \frac{2\pi\gamma_\beta \mathrm{EKE_{bt}^{1/4}}}{\beta^{1/2}}, \tag{16}$$

where γ_β is an $O(1)$ empirical constant. In our simulations, as in O'Gorman and Schneider (2008) and Schneider and Liu (2009), the Rhines scale with $\gamma_\beta = 1.6$ provides a good fit to the energy-containing eddy length scale in midlatitudes poleward of 45°N/S (Fig. 14). Equatorward of 45°N/S, the Rhines scale is considerably smaller than the energy-containing eddy length scale. The meridionally averaged Rhine scale $\langle L_\beta \rangle$ over the region poleward of 26°N/S is roughly proportional to the meridionally averaged energy-containing eddy length $\langle L_e \rangle$ over the same region (Fig. 15a).

g. Rossby deformation radius

To understand what controls the eddy length scales in lower latitudes and to what degree an inverse energy cascade may occur, it is helpful to consider the Rossby deformation radius. In the extratropics, it may be defined as

$$L_x = \frac{2\pi\gamma_x c}{|f|}, \tag{17}$$

where γ_x is an $O(1)$ empirical constant, which we chose to be 1.8 in our simulations as in Schneider and Liu (2009). The gravity wave speed c can be determined from the thermal stratification:

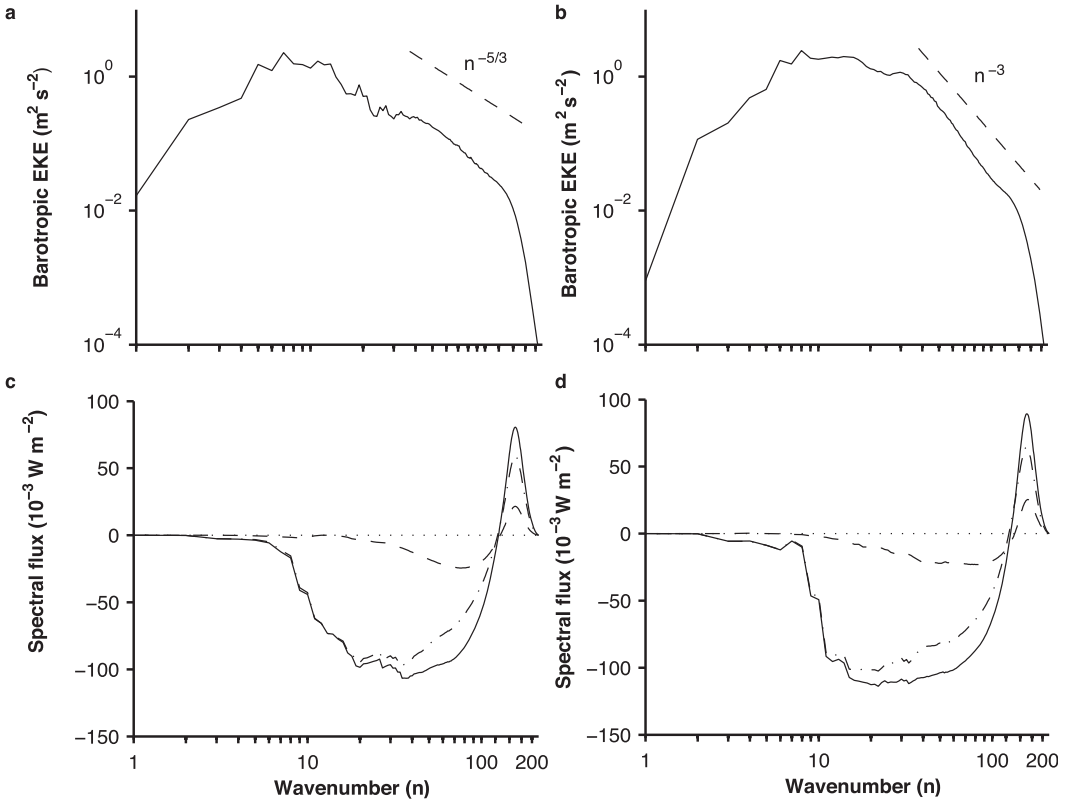

FIG. 11. (a),(b) Global barotropic EKE spectra and (c),(d) nonlinear spectral energy fluxes as a function of spherical wavenumber n. Simulations with (a),(c) strong ($\tau_0 = 10$ d) and (b),(d) weak bottom drag ($\tau_0 = 100$ d). The nonlinear spectral fluxes of total (globally integrated) kinetic energy (solid) are decomposed into fluxes owing to eddy–mean flow interactions (dashed–dotted) and eddy–eddy interactions (dashed) (Boer 1983).

$$c = \int_{p_t}^{p_s} N_p \, dp, \tag{18}$$

where p_s is the pressure at the lower boundary, p_t is the upper boundary of the integration, and $N_p^2 = -(\overline{\rho}\overline{\theta})^{-1}\overline{\partial_p \theta}$ (density ρ and potential temperature θ) is a static stability measure in pressure coordinates. Because the static stability is weak in the (nearly) neutrally stratified lower layers, the so-determined gravity wave speed depends only weakly on the lower boundary of the integration. However, it decreases as the upper boundary is lowered (p_t is increased) within the stably stratified upper troposphere. In our simulations, we chose the lower boundary of the integration to be $\sigma = 1.0$ (bottom of the domain), and we chose the upper boundary to be $p_t = 0.1$ bar, which is close to the tropopause.

The resulting extratropical Rossby deformation radius is an estimate of the length scale of the baroclinically most unstable linear waves. The Rossby deformation radius averaged over the region poleward of 26°N/S, $\langle L_x \rangle$, slightly increases as the drag time scale increases; it only shows large variations in simulations with very long drag time scales (Fig. 15b).

The equatorial Rossby deformation radius defined as $L_0 = (c/\beta)^{1/2}$ is approximately equal to the energy-containing eddy length scale in the equatorial region. As the drag time scale changes from 10 to 100 d, both length

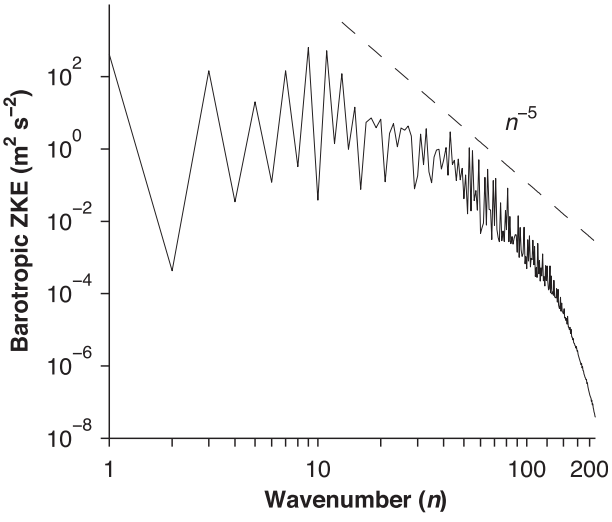

FIG. 12. Barotropic zonal kinetic energy spectrum ($m = 0$) for the simulation with $\tau_d = 100$ d.

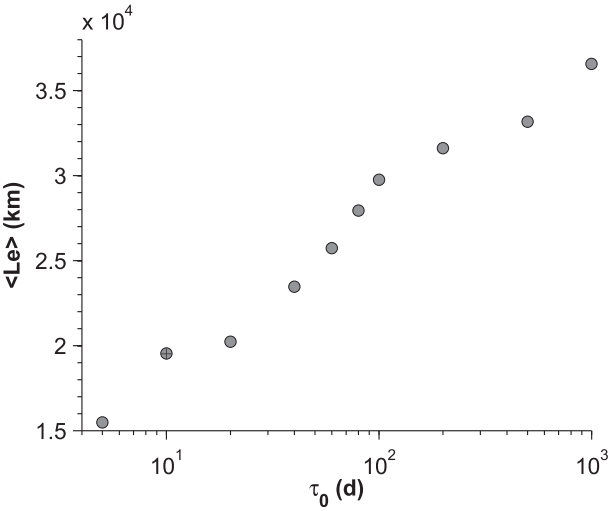

FIG. 13. Meridionally averaged energy-containing eddy length scale $\langle L_e \rangle$ over the region poleward of 26°N/S vs drag time scale τ_0.

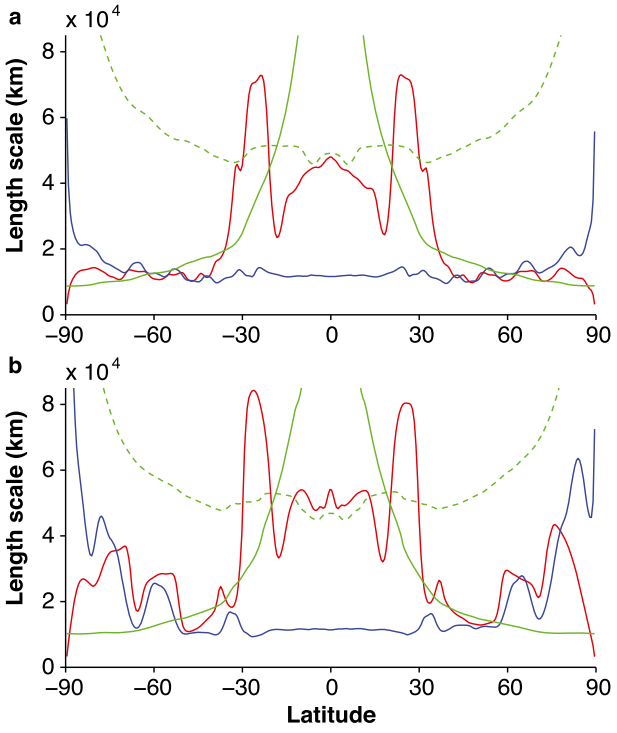

FIG. 14. Zonal wave lengths as a function of latitude. Simulation with (a) strong (τ_0 = 10 d) and (b) weak drag (τ_0 = 100 d). Red: energy-containing wavelength L_e. Blue: Rhines scale L_β. Green solid: extratropical Rossby deformation radius L_x. Green dashed: equatorial Rossby deformation radius L_0.

scales remain near 5×10^4 km (Fig. 14). Thus, like the energy-containing eddy length scale in the equatorial region, the equatorial Rossby deformation radius is not sensitive to variations of the off-equatorial drag, as the equatorial thermal stratification is largely unaffected by it.

6. Discussion and conclusions

We have presented a set of GCM simulations with flow parameters representative of Jupiter's atmosphere. We varied an off-equatorial bottom drag time scale (inverse drag coefficient) over a wide range (5–1000 d) to examine how jet and turbulence characteristics depend on it. As the drag time scale increased (drag coefficient decreased), the off-equatorial jets became stronger and wider, with increasing interjet spacing. At the same time, large coherent vortices on the flanks of the jets became more prevalent; the vortex lifespans were similar to the drag time scale. But although the flows varied strongly with the drag coefficient, the thermal structure of the atmosphere remained largely unchanged.

The strengthening of the zonal jets with decreasing drag coefficient can be understood qualitatively from the angular momentum budget. Integrated along an angular momentum surface, any net eddy angular momentum flux convergence and divergence must balance the frictional torque acting on the zonal flow in the drag layer. Since the eddy angular momentum flux convergence and divergence are concentrated in the upper troposphere and, like the atmospheric thermal structure, do not vary strongly with the drag coefficient, the zonal flow in the drag layer strengthens as the drag coefficient decreases to provide a frictional torque that can continue to balance the upper-tropospheric eddy angular momentum transport. Because the thermal wind shear does not change strongly with the drag coefficient, the jets in the upper atmosphere strengthen in proportion to the zonal flow in the drag layer; that is, the barotropic component of the zonal flow strengthens as the drag coefficient decreases, while the baroclinic component remains largely unchanged.

Analysis of the energy budget of the simulations indicates that the generation rate of potential energy $G(P)$ is approximately equal to the baroclinic conversion rate from potential energy to kinetic energy $C(P, K)$, and the kinetic energy dissipation rate associated with bottom drag $D(K)$ is approximately equal to the barotropic conversion rate from eddy to mean-flow kinetic energy $C(K_E, K_M)$, as anticipated by the Lorenz energy cycle (Lorenz 1955). But remarkably, the generation rate of potential energy, the energy conversion rates, and the energy dissipation rate by friction all remain essentially constant across the simulations. This suggests that the thermodynamic efficiency of the atmosphere is not sensitive to the drag coefficient. Based on the simulations and consistent

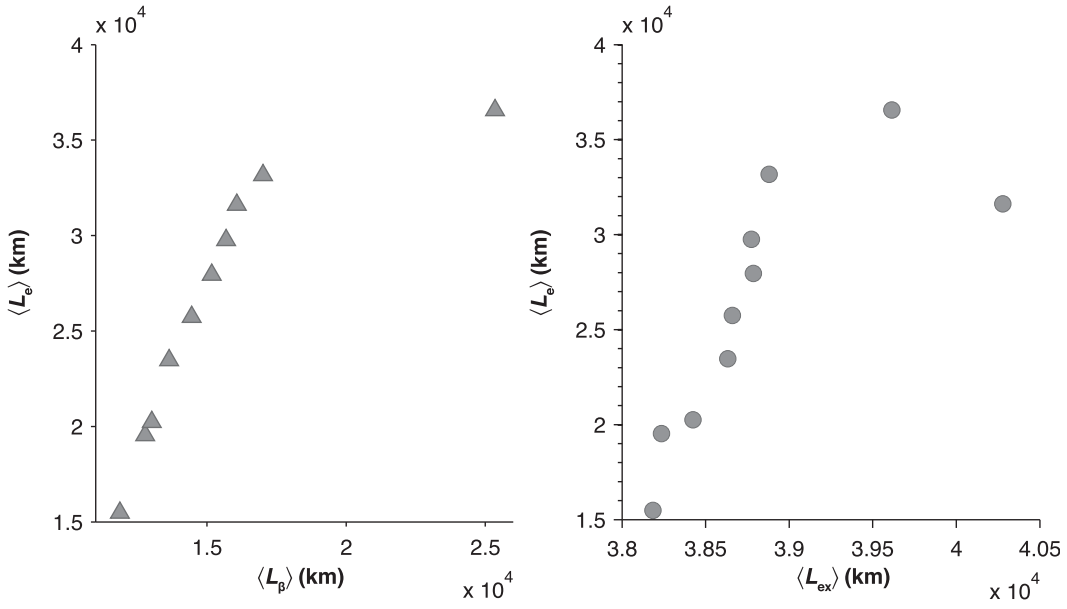

FIG. 15. Energy-containing eddy length scale vs (a) Rhines scale and (b) extratropical Rossby radius. All length scales are averaged over the region poleward of 26°N/S.

with available observations (Salyk et al. 2006), we estimate the thermodynamic efficiency of Jupiter's atmosphere to be about 2.7%. The near constancy of the barotropic conversion rate implies that the speeds of the prograde zonal jets scale with the square root of the drag time scale, while the speeds of the retrograde jets are limited by barotropic instability and hence are weaker.

The drag coefficient also influences turbulence characteristics of the simulated atmospheres. As the drag coefficient decreases, the barotropic component of EKE increases, while the baroclinic component of EKE remains relatively constant. In all simulations, the barotropic component of EKE dominates. In simulations with larger drag coefficients, the barotropic eddy kinetic energy spectrum has a range exhibiting an $n^{-5/3}$ power law in spherical wavenumber n. In simulations with smaller drag coefficients, it is closer to an n^{-3} power law. The flattening of the eddy kinetic energy spectrum to $n^{-5/3}$ as the drag coefficient increases might indicate the existence of an inverse energy cascade. However, the increasing dominance of barotropic EKE as the drag coefficient decreases would suggest any inverse energy cascade to be more prominent for smaller drag coefficients (Held and Larichev 1996). Examination of the zonal wavenumber spectra suggests any inverse cascade is limited to the equatorial region, where the spectra are relatively flat (close to a $-5/3$ power law), while the spectra in the off-equatorial region are steeper (close to a -3 power law). So the flattening of the global EKE spectrum as the drag coefficient increases may simply indicate the increasing dominance of equatorial turbulence (which is largely unaffected by the off-equatorial drag coefficient) over off-equatorial turbulence (which gets weaker as the drag coefficient increases). In all simulations, the kinetic energy of the zonal-mean flows is larger than the eddy kinetic energy. The zonal kinetic energy spectrum closely follows an n^{-5} power law. It indicates that the simulations are close to what Galperin et al. (2014) refer to as the zonostrophic regime, which is also observed on Jupiter. The eddy length scale increases with decreasing drag coefficient, and scales with the Rhines scale. The Rossby deformation radius is of the same order as the Rhines scale in the simulations, but it varies much less than the Rhines scale or the energy-containing scale as the drag coefficient is varied, consistent with the near constancy of the thermal structure.

The simulation results imply that the stronger and wider zonal jets on Saturn than on Jupiter may be the result of weaker MHD drag on Saturn. Given that the simulation results suggest that the speeds of the prograde jets are proportional to the square root of the drag time scale, the 3–6-times-stronger zonal wind speeds on Saturn indicate an effective drag time scale that is 10–40 longer on Saturn than on Jupiter. Since the drag time scale is proportional to the density where the drag occurs and is inversely proportional to the electrical conductivity and square of the magnetic field strength, weaker magnetic fields on Saturn with different combinations of electrical conductivities and depth of the layer where drag

occurs may account for weaker drag on Saturn. Forthcoming observations from the National Aeronautics and Space Administration's (NASA) Juno and Cassini missions may further constrain the depth of the magnetic drag and hence the strength of the drag on Jupiter and Saturn (Kaspi et al. 2010; Kaspi 2013; Liu et al. 2013, 2014). The weaker effective drag coefficient on Saturn may have observable consequences. For example, barotropic eddy kinetic spectrum on Saturn may be closer to an n^{-3} power law rather than the $n^{-5/3}$ power law observed on Jupiter (Choi and Showman 2011) and seen in our simulations with smaller drag coefficients.

Acknowledgments. This work was supported by the NASA Outer Planets Research Program (Grant NNX10AQ05G) and by the National Science Foundation (Grant AGS-1049201).

APPENDIX

Magnetohydrodynamic (MHD) Drag

Where the electrical conductivity is high in planetary atmospheres, the interaction of flows with magnetic fields generates Lorentz forces and associated Ohmic dissipation, which plays important roles in slowing down atmospheric flows (Liu et al. 2008; Perna et al. 2010; Rogers and Showman 2014), in heating the planetary interior (Batygin and Stevenson 2010), and in controlling the evolution of the planets (Batygin et al. 2011). For the atmospheres of hot Jupiters, the interactions of flows with magnetic fields have been studied using kinematic parameterizations of the magnetic field (Perna et al. 2010) and using full MHD simulations (Batygin et al. 2013; Rogers and Showman 2014). The full MHD simulations showed that these interactions indeed act as a drag and retard the flow. The flow retardation in the full MHD simulations is one order of magnitude smaller than in corresponding kinematic drag parameterizations, and it is more localized. However, the details of the magnetic drag depend on the flow and likely vary case by case. For our purposes—studying fundamental aspects of drag on giant planet flows—using a kinematic drag parameterization suffices.

In the momentum equation, the Lorentz force is

$$\mathbf{F}_L = \frac{\mathbf{J}\times\mathbf{B}}{\rho}, \tag{A1}$$

where $\mathbf{B}$ is the magnetic field and $\mathbf{J} = \sigma(\mathbf{u}\times\mathbf{B} + \mathbf{E})$ is the electric current density, with $\mathbf{E}$ being the electric field and σ the electrical conductivity. Given the continuity of the electric current density in the planetary interior, $\nabla\cdot\mathbf{J} = 0$, we have

$$\nabla\cdot\sigma\mathbf{E} = -\nabla\cdot\sigma(\mathbf{u}\times\mathbf{B}). \tag{A2}$$

For an exponentially varying electric conductivity, Batygin and Stevenson (2010) gave analytical solutions of the electrical field $\mathbf{E}$ for simplified magnetic field and flow configurations and showed that $\mathbf{E}\sim\mathbf{u}\times\mathbf{B}$, as constrained by the boundary conditions. Thus, dimensional arguments suggest that the Lorentz force scales as

$$\mathbf{F}_L \sim \frac{\sigma(\mathbf{u}\times\mathbf{B})\times\mathbf{B}}{\rho} \sim -\frac{\sigma\mathbf{u}B^2}{\rho} = -\frac{\mathbf{u}}{\tau}. \tag{A3}$$

Thus, the effect of the Lorentz force can be approximated as a Rayleigh drag with the time scale (Batygin et al. 2011)

$$\tau_d \sim \frac{\rho_d}{\sigma_d B_d^2}, \tag{A4}$$

where σ_d and B_d are the magnitudes of the electrical conductivity and magnetic field in the drag layer. For Jupiter, at $0.9R_J$, the density is about $100\,\mathrm{kg\,m^{-3}}$, and the electrical conductivity is about $4\times10^2\,\mathrm{S\,m^{-2}}$. The magnetic field in the interior is poorly constrained observationally. If we take the magnetic field to be the downward continuation of the observed magnetic field $B\approx5$ gauss (G; $1\,\mathrm{G} = 10^{-4}\,\mathrm{T}$), the derived Rayleigh drag time scale is about 10 d. However, the time scale varies strongly under different assumptions for the magnetic field strength and depth at which drag occurs. For example, if the magnitude of the magnetic field in the drag layer is ~3 times larger than the downward continuation of the observed magnetic field, the estimated Rayleigh drag time scale would be 1 d. For Saturn, the region of high electrical conductivity lies deeper in the planet (Liu et al. 2014). If we assume the density and electrical conductivity in the drag region for Saturn are similar to those for Jupiter, and if we also take the magnetic field to be the downward continuation of the observed magnetic field $B\approx0.25$ G, the Rayleigh drag time scale for Saturn can be as much as 400 times longer than that for Jupiter. But again, these estimates are sensitivities to assumptions about the depth of the drag that are poorly constrained observationally. Varying assumptions slightly, they can easily be reconciled with the finding of our simulations—that the effective drag time scale on Saturn is 10–40 longer than that on Jupiter.

REFERENCES

Batygin, K., and D. J. Stevenson, 2010: Inflating hot Jupiters with Ohmic dissipation. *Astrophys. J., Lett.,* **714,** L238–L243, doi:10.1088/2041-8205/714/2/L238.

——, ——, and P. H. Bodenheimer, 2011: Evolution of Ohmically heated hot Jupiters. *Astrophys. J.,* **738,** 1, doi:10.1088/0004-637X/738/1/1.

——, S. Stanley, and D. J. Stevenson, 2013: Magnetically controlled circulation on hot extrasolar planets. *Astrophys. J.,* **776,** 53, doi:10.1088/0004-637X/776/1/53.

Boer, G. J., 1983: Homogenous and isotropic turbulence on the sphere. *J. Atmos. Sci.,* **40,** 154–163, doi:10.1175/1520-0469(1983)040<0154:HAITOT>2.0.CO;2.

——, and T. G. Shepherd, 1983: Large-scale two-dimensional turbulence in the atmosphere. *J. Atmos. Sci.,* **40,** 164–183, doi:10.1175/1520-0469(1983)040<0164:LSTDTI>2.0.CO;2.

Choi, D. S., and A. P. Showman, 2011: Power spectral analysis of Jupiter's clouds and kinetic energy from *Cassini*. *Icarus,* **216,** 597–609, doi:10.1016/j.icarus.2011.10.001.

Connerney, J. E. P., 1993: Magnetic fields of the outer planets. *J. Geophys. Res.,* **98** (E10), 18 659–18 679, doi:10.1029/93JE00980.

Danilov, S., and D. Gurarie, 2002: Rhines scale and spectra of the β-plane turbulence with bottom drag. *Phys. Rev.,* **65E,** 067301, doi:10.1103/PhysRevE.65.067301.

Del Genio, A. D., and J. M. Barbara, 2012: Constrains on Saturn's tropospheric general circulation from Cassini ISS images. *Icarus,* **219,** 689–700, doi:10.1016/j.icarus.2012.03.035.

——, ——, J. Ferrier, A. P. Ingersoll, R. A. West, A. R. Vasavasa, J. Spitale, and C. C. Porco, 2007: Saturn eddy momentum fluxes and convection: First estimates from Cassini images. *Icarus,* **189,** 479–492, doi:10.1016/j.icarus.2007.02.013.

French, M., A. Becker, W. Lorenzen, N. Nettelmann, M. Bethkenhagen, J. Wicht, and R. Redmer, 2012: Ab initio simulations for material properties along the Jupiter adiabat. *Astrophys. J.,* **202** (Suppl.), 5, doi:10.1088/0067-0049/202/1/5.

Galperin, B., S. Sukoriansky, and H. Huang, 2001: Universal n^{-5} spectrum of zonal flows on giant planets. *Phys. Fluids,* **13,** 1545–1548, doi:10.1063/1.1373684.

——, ——, N. Dikovskaya, P. L. Read, Y. H. Yamazaki, and R. Wordworth, 2006: Anisotropic turbulence and zonal jets in rotating flows with a β-effect. *Nonlinear Processes Geophys.,* **13,** 83–98, doi:10.5194/npg-13-83-2006.

——, R. M. B. Young, S. Sukoriansky, N. Dikovskaya, P. L. Read, A. J. Lancaster, and D. Armstrong, 2014: Cassini observations reveal a regime of zonostrophic macroturbulence on Jupiter. *Icarus,* **229,** 295–320, doi:10.1016/j.icarus.2013.08.030.

Green, J. S. A., 1970: Transfer properties of the large-scale eddies and the general circulation of the atmosphere. *Quart. J. Roy. Meteor. Soc.,* **96,** 157–185, doi:10.1002/qj.49709640802.

Grote, E., and F. H. Busse, 2001: Dynamics of convection and dynamos in rotating spherical fluid shells. *Fluid Dyn. Res.,* **28,** 349–368, doi:10.1016/S0169-5983(01)00004-1.

Guillot, T., 2005: The interiors of giant planets: Models and outstanding questions. *Annu. Rev. Earth Planet. Sci.,* **33,** 493–530, doi:10.1146/annurev.earth.32.101802.120325.

——, D. J. Stevenson, W. B. Hubbard, and D. Saumon, 2004: The interior of Jupiter. *Jupiter: The Planet, Satellites and Magnetosphere,* F. Bagenal, T. E. Dowling, and W. B. McKinnon, Eds., Cambridge University Press, 35–57.

Gurnett, D., A. Persoon, W. Kurth, J. Groene, T. Averkamp, M. Dougherty, and D. Southwood, 2007: The variable rotation period of the inner region of Saturn's plasma disk. *Science,* **316,** 442–445, doi:10.1126/science.1138562.

Haynes, P. H., C. J. Marks, M. E. McIntyre, T. G. Shepherd, and K. P. Shine, 1991: On the downward control of extratropical diabatic circulations by eddy-induced mean zonal forces. *J. Atmos. Sci.,* **48,** 651–679, doi:10.1175/1520-0469(1991)048<0651:OTCOED>2.0.CO;2.

Heimpel, M., and N. Gómez Pérez, 2011: On the relationship between zonal jets and dynamo action in giant planets. *Geophys. Res. Lett.,* **38,** L14201, doi:10.1029/2011GL047562.

——, J. Aurnou, and J. Wicht, 2005: Simulation of equatorial and high-latitude jets on Jupiter in a deep convection model. *Nature,* **438,** 193–196, doi:10.1038/nature04208.

Held, I. M., and M. J. Suarez, 1994: A proposal for the intercomparison of the dynamical cores of atmospheric general circulation models. *Bull. Amer. Meteor. Soc.,* **75,** 1825–1830, doi:10.1175/1520-0477(1994)075<1825:APFTIO>2.0.CO;2.

——, and V. D. Larichev, 1996: A scaling theory for horizontally homogenous, baroclinically unstable flow on a beta plane. *J. Atmos. Sci.,* **53,** 946–952, doi:10.1175/1520-0469(1996)053<0946:ASTFHH>2.0.CO;2.

Ingersoll, A. P., R. F. Beebe, J. L. Mitchell, G. W. Garneau, G. M. Yagi, and J.-P. Müller, 1981: Interaction of eddies and mean zonal flow on Jupiter as inferred from Voyager 1 and 2 images. *J. Geophys. Res.,* **86,** 8733–8743, doi:10.1029/JA086iA10p08733.

James, I., and L. J. Gray, 1986: Concerning the effect of surface drag on the circulation of a baroclinic planetary atmosphere. *Quart. J. Roy. Meteor. Soc.,* **112,** 1231–1250, doi:10.1002/qj.49711247417.

Kaspi, Y., 2013: Inferring the depth of the zonal jets on Jupiter and Saturn from the odd gravity harmonics. *Geophys. Res. Lett.,* **40,** 676–680, doi:10.1029/2012GL053873.

——, G. R. Flierl, and A. P. Showman, 2009: The deep wind structure of the giant planets: Results from an anelastic general circulation model. *Icarus,* **202,** 525–542, doi:10.1016/j.icarus.2009.03.026.

——, W. B. Hubbard, A. P. Showman, and G. R. Flierl, 2010: Gravitational signature of Jupiter's internal dynamics. *Geophys. Res. Lett.,* **37,** L01204, doi:10.1029/2009GL041385.

Liu, J. J., and T. Schneider, 2010: Mechanisms of jet formation on giant planets. *J. Atmos. Sci.,* **67,** 3652–3672, doi:10.1175/2010JAS3492.1.

——, and ——, 2011: Convective generation of equatorial super rotation in planetary atmospheres. *J. Atmos. Sci.,* **68,** 2742–2755, doi:10.1175/JAS-D-10-05013.1.

——, P. M. Goldreich, and D. J. Stevenson, 2008: Constraints on deep-seated zonal winds inside Jupiter and Saturn. *Icarus,* **196,** 653–664, doi:10.1016/j.icarus.2007.11.036.

——, T. Schneider, and Y. Kaspi, 2013: Predictions of thermal and gravitational signals of Jupiter's deep zonal winds. *Icarus,* **224,** 114–125, doi:10.1016/j.icarus.2013.01.025.

——, ——, and L. N. Fletcher, 2014: Constraining the depth of Saturn's zonal winds by measuring thermal and gravitational signals. *Icarus,* **239,** 260–272, doi:10.1016/j.icarus.2014.05.036.

Lorenz, E. N., 1955: Available potential energy and the maintenance of the general circulation. *Tellus,* **7,** 157–167, doi:10.1111/j.2153-3490.1955.tb01148.x.

Magalhães, J. A., A. Seiff, and R. E. Young, 2002: The stratification of Jupiter's troposphere at the Galileo probe entry site. *Icarus,* **158,** 410–433, doi:10.1006/icar.2002.6891.

Nellis, W. J., A. C. Mitchell, P. McCandless, D. J. Erskine, and S. T. Weir, 1992: Electronic energy gap of molecular hydrogen from electrical conductivity measurements at high shock pressures. *Phys. Rev. Lett.,* **68,** 2937–2940, doi:10.1103/PhysRevLett.68.2937.

——, S. T. Weir, and A. C. Mitchell, 1996: Metallization and electrical conductivity of hydrogen in Jupiter. *Science,* **273,** 936–938, doi:10.1126/science.273.5277.936.

O'Gorman, P. A., and T. Schneider, 2008: Weather-layer dynamics of baroclinic eddies and multiple jets in an idealized general circulation model. *J. Atmos. Sci.,* **65,** 524–535, doi:10.1175/2007JAS2280.1.

Pauluis, O., and J. Dias, 2012: Satellite estimation of precipitation-induced dissipation in the atmosphere. *Science,* **335,** 953–956, doi:10.1126/science.1215869.

Peixoto, J. P., and A. H. Oort, 1992: *Physics of Climate*. American Institute of Physics, 555 pp.

Perna, R., K. Menou, and E. Rauscher, 2010: Magnetic drag on hot Jupiter atmospheric winds. *Astrophys. J.,* **719,** 1421–1426, doi:10.1088/0004-637X/719/2/1421.

Porco, C. C., and Coauthors, 2003: Cassini imaging of Jupiter's atmosphere, satellites, and rings. *Science,* **299,** 1541–1547, doi:10.1126/science.1079462.

Rhines, P. B., 1975: Waves and turbulence on a beta-plane. *J. Fluid Mech.,* **69,** 417–443, doi:10.1017/S0022112075001504.

——, 1994: Jets. *Chaos,* **4,** 313–339, doi:10.1063/1.166011.

Rogers, T. M., and A. P. Showman, 2014: Magnetohydrodynamic simulations of the atmosphere of HD 209458b. *Astrophys. J.,* **782,** L4, doi:10.1088/2041-8205/782/1/L4.

Salyk, C., A. P. Ingersoll, J. Lorre, A. Vasavada, and A. D. Del Genio, 2006: Interaction between eddies and mean flow in Jupiter's atmosphere: Analysis of Cassini imaging data. *Icarus,* **185,** 430–442, doi:10.1016/j.icarus.2006.08.007.

Sardeshmukh, P. D., and B. J. Hoskins, 1988: The generation of global rotational flow by steady idealized tropical divergence. *J. Atmos. Sci.,* **45,** 1228–1251, doi:10.1175/1520-0469(1988)045<1228:TGOGRF>2.0.CO;2.

Schneider, T., and C. C. Walker, 2006: Self-organization of atmospheric macroturbulence into critical states of weak nonlinear eddy–eddy interactions. *J. Atmos. Sci.,* **63,** 1569–1586, doi:10.1175/JAS3699.1.

——, and ——, 2008: Scaling laws and regime transitions of macroturbulence in dry atmospheres. *J. Atmos. Sci.,* **65,** 2153–2173, doi:10.1175/2007JAS2616.1.

——, and J. J. Liu, 2009: Formation of jets and equatorial superrotation on Jupiter. *J. Atmos. Sci.,* **66,** 579–601, doi:10.1175/2008JAS2798.1.

Scott, R. K., and D. G. Dritschel, 2013: Halting scale and energy equilibration in two-dimensional quasigeostrophic turbulence. *J. Fluid Mech.,* **721,** R4, doi:10.1017/jfm.2013.120.

Simmons, A., and B. Hoskins, 1976: Baroclinic instability on the sphere: Normal modes of the primitive and quasi-geostropic equations. *J. Atmos. Sci.,* **33,** 1454–1477, doi:10.1175/1520-0469(1976)033<1454:BIOTSN>2.0.CO;2.

——, and ——, 1977: Baroclinic instability on the sphere: Solutions with a more realistic tropopause. *J. Atmos. Sci.,* **34,** 581–588, doi:10.1175/1520-0469(1977)034<0581:BIOTSS>2.0.CO;2.

Smith, K. S., G. Boccaletti, C. C. Henning, I. Marinov, C. Y. Tam, I. M. Held, and G. K. Vallis, 2002: Turbulent diffusion in the geostrophic inverse cascade. *J. Fluid Mech.,* **469,** 13–48, doi:10.1017/S0022112002001763.

Thompson, A. F., and W. R. Young, 2007: Two-layer baroclinic eddy heat fluxes: Zonal flows and energy balance. *J. Atmos. Sci.,* **64,** 3214–3231, doi:10.1175/JAS4000.1.

Vallis, G. K., 2006: *Atmospheric and Oceanic Fluid Dynamics: Fundamentals and Large-Scale Circulation.* Cambridge University Press, 771 pp.

Williams, P. D., 2011: The RAW filter: An improvement to the Robert–Asselin filter in semi-implicit integrations. *Mon. Wea. Rev.,* **139,** 1996–2007, doi:10.1175/2010MWR3601.1.